

Relative Transverse Momentum Distributions of Bottom Hadrons Produced in 1.96 TeV Proton-Antiproton Collisions

by
Philippe Roy

Submitted in partial fulfillment of the
requirements for the degree of
Master of Science

Department of Physics

McGill University

Montreal, Quebec

2008-05-02

Requirements Statement

Copyright Statement

DEDICATION

To all the people courageous enough to read this thesis entirely.

ACKNOWLEDGEMENTS

I thank Andreas T. Warburton, my supervisor, and Richard J. Tesarek; without them this project would not have been possible. I also thank Elena Vataga for much great advice throughout this perilous journey. I thank Robert Snihur for his technical support and Pierre-Hugues Beauchemin for his distracting presence. I also thank Miika Klemetti for putting up with me every working day of the week, and I finally thank Norma Cenva who proved to us that appearance isn't everything.

ABSTRACT

Fragmentation is the process by which bare quarks dress themselves up as hadrons. Since we cannot get reliable calculations of this process using perturbative quantum chromodynamics, the fragmentation properties of quarks must be obtained empirically. We report on the signal extraction and relative transverse momentum (p_T) spectrum determination that will lead to a high precision measurement of relative fragmentation fractions of b quarks into B hadrons, in 1.96 TeV $p\bar{p}$ collisions. Using 1.9 fb^{-1} of data taken with the CDF-II detector, we fully reconstruct 473 ± 42 $B_s^0 \rightarrow D_s^- \pi^+$, 15206 ± 203 $B^0 \rightarrow D^- \pi^+$, 1483 ± 45 $B^0 \rightarrow D^{*-} \pi^+$ and 4444 ± 297 $\Lambda_b^0 \rightarrow \Lambda_c^+ \pi^-$ candidate decays. In order to reduce systematic uncertainties, ratios of p_T spectra are reported. We find that B_s and B^0 mesons are produced with similar p_T and Λ_b baryons are produced with lower p_T than B^0 mesons. Our results are consistent with previous CDF measurements suggesting a difference between fragmentation processes observed at lepton and hadron colliders.

ABRÉGÉ

La fragmentation est le procédé par lequel les quarks se déguisent en hadrons. Puisque nous ne pouvons obtenir de calculs fiables de ce procédé en utilisant la chromodynamique quantique perturbative, les propriétés de fragmentation des quarks doivent être obtenues expérimentalement. Nous discutons de l'extraction de signaux et de la détermination de spectres de quantité de mouvement (p_T) relatifs qui nous mèneront à une mesure précise de fractions de fragmentation relatives des quarks de type b aux hadrons de type B , utilisant des collisions de protons-antiprotons à une énergie de centre-de-masse de 1.96 TeV. Utilisant 1.9 fb^{-1} de données prises avec le détecteur CDF-II, nous faisons une reconstruction complète de $473 \pm 42 B_s^0 \rightarrow D_s^- \pi^+$, $15206 \pm 203 B^0 \rightarrow D^- \pi^+$, $1483 \pm 45 B^0 \rightarrow D^{*-} \pi^+$ et $4444 \pm 297 \Lambda_b^0 \rightarrow \Lambda_c^+ \pi^-$ candidats à la désintégration. De façon à réduire les incertitudes de type systématique, nous mesurons des rapports de spectres de p_T . Nous trouvons que les mesons B_s et B^0 sont produits avec des p_T similaires alors que les baryons Λ_b sont produits avec des p_T plus bas que ceux des mesons B^0 . Nos résultats se conforment à des résultats obtenus antérieurement par la collaboration CDF, suggérant une différence entre les procédés de fragmentation aux collisionneurs de leptons et à ceux de hadrons.

TABLE OF CONTENTS

DEDICATION		ii
ACKNOWLEDGEMENTS		iii
ABSTRACT		iv
ABRÉGÉ		v
LIST OF TABLES		viii
LIST OF FIGURES		ix
1	Introduction	1
1.1	Introduction	1
1.2	QCD	3
1.3	Fragmentation	3
2	Experimental Apparatus	10
2.1	The Fermilab National Accelerator Complex Laboratory	11
2.2	The Collider Detector at Fermilab	12
2.3	Tracking Systems	14
2.3.1	Central Outer Tracker	15
2.3.2	Track Reconstruction	18
2.3.3	Pattern Recognition Algorithms	19
2.4	Trigger System	21
3	Skimming of the datasets	26
3.1	Trigger and Data Sample	26
3.2	Selection Requirements	27
3.3	Signal Reconstruction	28
3.3.1	D_s^+ Reconstruction	29
3.3.2	D^+ and Λ_c^+ Reconstruction	31

3.3.3	D^{*+} Reconstruction	31
3.3.4	B Hadron Reconstruction	33
3.3.5	B Hadron Mass Fit	38
3.3.6	Data Quality	39
3.4	Summary	39
4	Signal Optimization and Yields	42
4.1	B Hadron Invariant Mass Fit	43
4.1.1	$B_s^0 \rightarrow D_s^- \pi^+$ Fit	45
4.1.2	$B^0 \rightarrow D^- \pi^+$ Fit	49
4.1.3	$B^0 \rightarrow D^{*-} \pi^+$ Fit	55
4.1.4	$\Lambda_b^0 \rightarrow \Lambda_c^+ \pi^-$ Fit	58
5	Results	67
5.1	Extracting the p_T spectra	67
5.1.1	$B_s^0 \rightarrow D_s^- \pi^+$ p_T spectrum	68
5.1.2	$B^0 \rightarrow D^- \pi^+$ p_T spectrum	74
5.1.3	$B^0 \rightarrow D^{*-} \pi^+$ p_T spectra	79
5.1.4	$\Lambda_b^0 \rightarrow \Lambda_c^+ \pi^-$ p_T spectra	83
5.2	Systematics	85
5.3	Monte Carlo	85
5.4	Results	88
6	Conclusion	92
6.1	Future Work	93
	REFERENCES	95

LIST OF TABLES

<u>Table</u>	<u>page</u>
3-1 Datasets used in skimming and relevant information.	27
4-1 $B_s \rightarrow D_s^- \pi^+$ mass spectrum floating fit parameters.	50
4-2 $B_s \rightarrow D_s^- \pi^+$ mass spectrum fixed fit parameters.	50
4-3 $B^0 \rightarrow D^- \pi^+$ mass spectrum floating fit parameters.	56
4-4 $B^0 \rightarrow D^- \pi^+$ mass spectrum fixed fit parameters.	56
4-5 $B^0 \rightarrow D^{*-} \pi^+$ mass spectrum floating fit parameters.	59
4-6 $B^0 \rightarrow D^{*-} \pi^+$ mass spectrum fixed fit parameters.	59
4-7 $\Lambda_b^0 \rightarrow \Lambda_c^+ \pi^-$ mass spectrum floating fit parameters.	66
4-8 $\Lambda_b^0 \rightarrow \Lambda_c^+ \pi^-$ mass spectrum fixed fit parameters.	66
5-1 $B_s \rightarrow D_s^- \pi^+$ “k” factors.	73
5-2 $B^0 \rightarrow D^- \pi^+$ “k” factors.	78
5-3 $B^0 \rightarrow D^{*-} \pi^+$ “k” factors.	81
5-4 $\Lambda_b^0 \rightarrow \Lambda_c^+ \pi^-$ “k” factors.	85

LIST OF FIGURES

<u>Figure</u>	<u>page</u>
1-1 Representation of a $p\bar{p}$ collision.	5
1-2 Topology of a Λ_b^0 decay.	7
1-3 Comparison of B^0 and Λ_b p_T spectra.	8
2-1 Fermilab accelerator complex.	10
2-2 Solid-cutaway view of the CDF-II detector.	13
2-3 Schematic of the CDF Run II silicon detector.	15
2-4 Layout of wire planes on a COT endplate.	16
2-5 Diagram of the CDF-II trigger system.	22
3-1 Block diagram of the skimming algorithm and a schematic of the B -hadron reconstruction.	28
3-2 $M(KK)$ and $M(KK\pi)$ distributions.	30
3-3 $M(K\pi\pi)$ and $M(pK\pi)$ distributions.	32
3-4 $M(K\pi)$ and $M(K\pi\pi)-M(K\pi)$ distributions.	34
3-5 $M(D_s\pi)$ distribution.	36
3-6 $M(D\pi)$ distribution.	36
3-7 $M(D^*\pi)$ distribution.	37
3-8 $M(\Lambda_c\pi)$ distribution.	37
3-9 D^+ yield, $M(D)$ mean and width vs run number.	40
4-1 Significance versus L_{xy} distribution for all four decay channels.	44

4-2	$D_s\pi$ invariant mass fit.	51
4-3	$D\pi$ invariant mass fit.	55
4-4	$D^*\pi$ invariant mass fit.	60
4-5	$\Lambda_c\pi$ invariant mass fit.	65
5-1	$D_s\pi$ invariant mass fit and fitting regions.	69
5-2	Raw p_T spectra for regions 1 to 4 in the $B_s^0 \rightarrow D_s^-\pi^+$ mode.	70
5-3	p_T spectrum for the partially reconstructed decays in the $B_s^0 \rightarrow D_s^-\pi^+$ mode.	72
5-4	p_T spectrum for the mis-reconstructed decays in the $B_s^0 \rightarrow D_s^-\pi^+$ mode.	72
5-5	B_s hadron p_T spectrum.	73
5-6	$D\pi$ invariant mass fit and fitting regions.	74
5-7	Raw p_T spectra for regions 1 to 4 in the $B^0 \rightarrow D^-\pi^+$ mode.	75
5-8	p_T spectrum for the partially reconstructed decays in the $B^0 \rightarrow D^-\pi^+$ mode.	77
5-9	p_T spectrum for the mis-reconstructed (MR) decays in the $B^0 \rightarrow D^-\pi^+$ mode.	77
5-10	p_T spectrum for the $B^0 \rightarrow D^-\pi^+$ hadron.	78
5-11	$D^*\pi$ invariant mass fit and fitting regions.	79
5-12	Raw p_T spectra for regions 1, 3 and 4 in the $B^0 \rightarrow D^{*-}\pi^+$ mode.	80
5-13	p_T spectrum for the partially reconstructed decays in the $B^0 \rightarrow D^{*-}\pi^+$ mode.	82
5-14	p_T spectrum for the $B^0 \rightarrow D^{*-}\pi^+$ hadron.	82
5-15	$\Lambda_c\pi$ invariant mass fit and fitting regions.	83
5-16	Raw p_T spectra for regions 1 to 4 in the $\Lambda_b^0 \rightarrow \Lambda_c^+\pi^-$ mode.	84

5-17 p_T spectrum for the partially reconstructed decays in the $\Lambda_b^0 \rightarrow \Lambda_c^+ \pi^-$ mode.	86
5-18 p_T spectrum for the mis-reconstructed decays in the $\Lambda_b^0 \rightarrow \Lambda_c^+ \pi^-$ mode.	86
5-19 Λ_b hadron p_T spectrum.	87
5-20 Ratios of B_s and B^0 p_T spectra for both MC and data.	88
5-21 Ratios of $B^0 \rightarrow D^* \pi$ and $B^0 \rightarrow D \pi$ p_T spectra for both MC and data.	89
5-22 Ratios of Λ_b and B^0 p_T spectra for both MC and data.	90

CHAPTER 1

Introduction

1.1 Introduction

The advent of the Standard Model (SM) of particle physics occurred with the development of electroweak theory in the early 1970s, which extended the theory of quantum electrodynamics (QED) [1] to include the weak interaction [2]. Following great success in predicting electroweak couplings and decay rates, the SM was extended to include the strong interaction with the development of quantum chromodynamics (QCD) in the mid-1970s. With the inclusion of the color field, the SM has proved to be remarkably robust. Moreover, QCD is also successful in its ability to make accurate predictions that are born out experimentally.

The SM is a theory based on the symmetry group $SU(3) \times SU(2) \times U(1)$. Both $SU(n)$ and $U(n)$ are Lie groups, *i.e.* any element of the group can be represented by m fundamental elements or generators [3]:

$$E = \exp \sum_i^m (\theta_i F_i), \tag{1.1}$$

where F_i is the i^{th} generator and θ^i is the rotation angle corresponding to each generator. Elements of the $SU(n)$ groups are represented by $n \times n$ unitary matrices, $U^\dagger U = 1$, with $\det U = +1$ and have n^2-1 generators. The $U(1)$ group describes the

electromagnetic interaction while the $SU(2)$ group describes the weak interaction; these are beyond the scope of this thesis.

The $SU(3)$ group describes the strong color interaction among quarks, mediated via the exchange of eight massless spin-1 gluons. Gluons are vector, gauge bosons that cause quarks to interact in QCD. The quarks carry three possible “chromo-electric charges” or “colors”: red, green and blue (R,G,B), which are analogous to the electric charge in the electromagnetic interaction. Gluons also carry color charge combinations, making it possible to interact with themselves, and are associated with the following color combinations:

$$R\bar{B}, R\bar{G}, B\bar{R}, B\bar{G}, G\bar{R}, G\bar{B}, \frac{(R\bar{R} - G\bar{G})}{\sqrt{2}} \quad \text{and} \quad \frac{(R\bar{R} + G\bar{G} - 2B\bar{B})}{\sqrt{6}}. \quad (1.2)$$

The strong interaction binds the quarks together to form a color singlet state, $q\bar{q}$ or qqq ($R\bar{R}$ or RGB). The $q\bar{q}$ bound state is referred to as “meson” and the qqq bound state is referred to as “baryon”. For example, a $\bar{b}d$ bound state is a B^0 meson and a udb bound state is a Λ_b baryon. Both mesons and baryons are called “hadrons”. Just as the residual electric field outside of the neutral atoms causes them to combine into molecules, the residual color field outside of the protons and neutrons causes them to form nuclei. Most fundamental particles have an associated antiparticle, *i.e.* of which the electric charge, color charge and flavor are reversed, but the mass and the spin are the same.

1.2 QCD

One of the most exciting challenges for particle physics is the study of the non-perturbative regime of QCD. It is this regime that is relevant for understanding how the elementary fields of QCD (quarks and gluons) build up particles such as protons and neutrons. A basic theoretical difficulty is the non-existence of isolated, colored objects. This is a feature of the richness of the vacuum structure of QCD. Understanding the different QCD phases and the transitions among them is the challenge of the modern study of strong interactions. At low energy, chiral symmetry can be used to build an effective theory of hadron interactions. At higher energies, the parton model uses non-perturbative quark and gluon distributions to describe hadronic scattering processes. The QCD confinement scale $\Lambda_{QCD} \approx 400\text{MeV}$ is the typical energy at which QCD becomes non-perturbative (NP) [4]. When one of the participating quarks of the interaction is much heavier than Λ_{QCD} , the theory greatly simplifies as the heavy quark acts as a static source of electromagnetic and color (chromomagnetic) fields. This theory is known as heavy quark effective theory (HQET) [5] [6] and is particularly useful in describing the spectroscopy of bottom hadrons. HQET states that, to first order, the spectrum of all B mesons is expected to be the same. Since bare quarks are not observed, they must combine with either an antiquark or two other quarks to form a hadron. The dressing of bare quarks to form hadrons is called fragmentation.

1.3 Fragmentation

Fragmentation is a QCD process that involves not only single partons, the point-like constituents of hadrons, but also a cascade of many partons. In our case, the

interaction between initial state partons that produces final state partons, or fundamental interaction, can be described by perturbative QCD (pQCD) calculations. On the other hand, a NP parameterization is needed to describe the dressing of the parton into a hadron, or fragmentation. Fragmentation is not well predicted by theory, and therefore needs to be measured experimentally. Many models [7] [8] [9] [10] [11] try to describe the NP effects of fragmentation. One of these models, by Peterson [9], states that fragmentation would be inversely proportional to the energy transferred from the heavy (b) quark to the B hadron [12]. One advantage of the Peterson parameterization is that it only depends on one experimental parameter ϵ_b , whose value was determined to be 0.006 ± 0.002 by Chrin in [13]. We note that this determination of ϵ_b was tuned using e^+e^- collisions. A study by the SLD collaboration at the Stanford Linear Accelerator Center (SLAC) actually excludes a number of models, Peterson's among them, from their data [14]. This thesis still makes use of the Peterson model as it is widely used in bottom physics.

The probabilities that the fragmentation of a b quark results in a \overline{B}^0 , \overline{B}_s^0 meson and a Λ_b^0 baryon, are defined as f_{B^0} , f_{B_s} and f_{Λ_b} , respectively. Since bare quarks are not observed, it is possible to measure such quantities because of asymptotic freedom. Asymptotic freedom is a feature of QCD in which the interaction between particles becomes arbitrarily weak at ever shorter distances. This implies that, at short distance scales or very high energies, the partons (quarks, gluons) in the hadron may be considered as free particles. Scattering at these high energies may be treated as the interactions between partons. A schematic of a typical interaction as seen by

the CDF-II Detector at the Fermilab National Accelerator Laboratory facility can be seen in Figure 1-1.

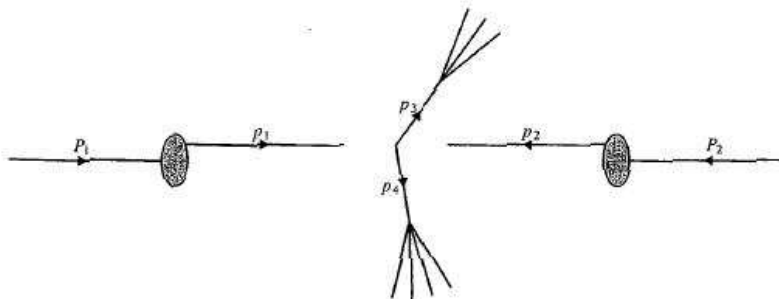


Figure 1-1: Representation of a $p\bar{p}$ collision.

The momenta of the incoming proton and antiproton are represented by P_1 and P_2 , respectively, while the incoming and outgoing parton momenta are p_1 , p_2 and p_3 , p_4 . In our case, the outgoing parton then fragments into a B hadron that decays into many particles that may be observed by the detector.

For this analysis, we are interested in the flavor and momentum dependence of the b -quark fragmentation process produced in hadronic $p\bar{p}$ collisions at $\sqrt{s} = 1.96$ TeV with the CDF-II detector. More specifically, we are interested in the following quantities:

$$\frac{\frac{d\sigma}{dp_T} (p\bar{p} \rightarrow \Lambda_b^0 X)}{\frac{d\sigma}{dp_T} (p\bar{p} \rightarrow B^0 X)} \quad (1.3)$$

and

$$\frac{\frac{d\sigma}{dp_T}(p\bar{p} \rightarrow B_s^0 X)}{\frac{d\sigma}{dp_T}(p\bar{p} \rightarrow B^0 X)}, \quad (1.4)$$

where

$$\sigma(p\bar{p} \rightarrow B^0 X) = \sigma(p\bar{p} \rightarrow b\bar{b}) \times f_d, \quad (1.5)$$

and similarly for the Λ_b^0 and B_s^0 cross sections. The differential cross sections ($\frac{d\sigma}{dp_T}$) are defined for $p_T > 6$ GeV/c. The above measurements will be made using fully reconstructed decay modes:

- $B_s^0 \rightarrow D_s^- \pi^+$, where $D_s^- \rightarrow \phi \pi^-$, $\phi \rightarrow K^+ K^-$;
- $B^0 \rightarrow D^- \pi^+$, where $D^- \rightarrow K^+ \pi^- \pi^-$;
- $\Lambda_b^0 \rightarrow \Lambda_c^+ \pi^-$, where $\Lambda_c^+ \rightarrow p K^- \pi^+$.

Charge conjugate modes are implied throughout this thesis. All the above decays have a four-track final state of the same topology. The topology of one of these decays, in this case a Λ_b^0 , is represented in Figure 1–2. We call these decays one prong-three prong (1-3) decays because only one track from the B -hadron vertex is seen in the detector while three tracks from the charm hadron are observed. Forming the ratios in equations 1.3 and 1.4 give us a measurement basically free of systematic uncertainties. Effects such as the $b\bar{b}$ production cross section and the reconstruction efficiency all cancel out because of the similarity between the decay modes we reconstruct. In order to better understand and constrain systematic uncertainties associated with the one prong vertex, we propose to use a fourth decay mode,

- $B^0 \rightarrow D^{*-} \pi^+$, where $D^{*-} \rightarrow \bar{D}^0 \pi^-$, $\bar{D}^0 \rightarrow K^+ \pi^-$.

This decay mode also has a four-track final state, but with a slightly different decay topology (2-2).

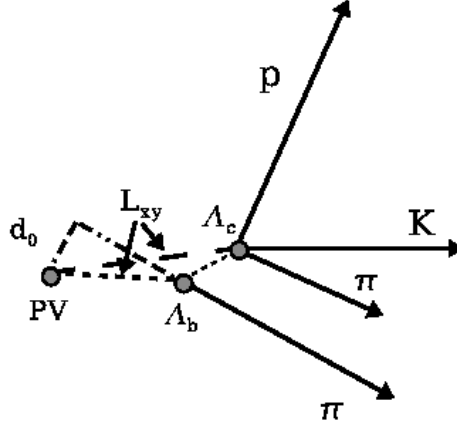


Figure 1–2: Topology of a Λ_b^0 decay. PV is the Primary Vertex of the interaction, L_{xy} defines the displacement of a vertex in the transverse plane and d_0 is the distance of closest approach of a track to the beamline.

The main motivation behind this measurement comes from the possible difference in b -baryon formation in hadronic collisions and in e^+e^- collisions. A discrepancy between the fragmentation fraction times branching ratio measurements from CDF [15] and LEP [16] [17] [18] was observed by Karen Gibson. LEP was an e^+e^- collider built near Geneva Switzerland by the *Conseil Européen pour la Recherche Nucléaire* (CERN). The observed discrepancy may indicate a difference in the fragmentation processes at hadron colliders, like the $p\bar{p}$ collisions we find at the Fermilab Tevatron, and e^+e^- colliders. The average transverse momentum of the B hadrons produced at LEP ($\langle p_T \rangle \sim 45 \text{ GeV}/c$) was also very different than the average p_T

of the B hadrons we study in this thesis ($\langle p_T \rangle \sim 15 \text{ GeV}/c$). The study of the momentum dependence of the b -quark fragmentation process may tell us more about this discrepancy. A similar momentum-dependent technique has already been used by Shin-Shan Yu [19] and it shows a difference between the B^0 and Λ_b p_T spectra in $p\bar{p}$ collisions. This discrepancy can be seen in Figure 1–3 [20]. We can see from this plot that the Λ_b baryon has a softer (lower on average) p_T spectrum than the B^0 meson, something that is not necessarily expected.

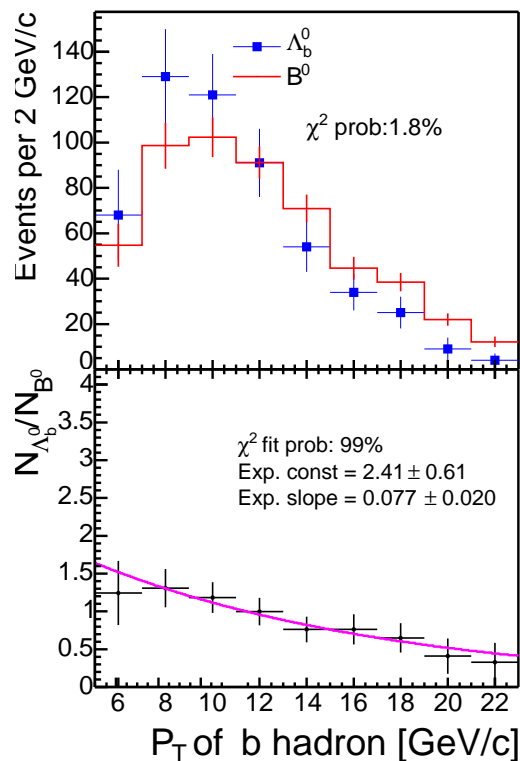


Figure 1–3: Comparison of B^0 and Λ_b p_T spectra [20] as measured by the Collider Detector at Fermilab in proton-antiproton collisions. The slope (approximately 3.8σ away from zero) of the ratio of Λ_b to B^0 histograms indicates that $p_T(B^0)$ is harder than $p_T(\Lambda_b)$.

Fragmentation of b quarks to B_s^0 mesons forms a critical input to the branching ratio of $B_s^0 \rightarrow \mu^+\mu^-$ ([21] [22]), as well as the $B_s^0 \rightarrow \mu^+\mu^-X$ ([23] [24] [25] [26]) sensitivity. Larger branching ratios than predicted by the Standard Model for these decay modes are indicators of physics not described by the SM. Improvement of this number improves the reliability of the rare decay sensitivity assessments and improves uncertainty when estimating branching fractions. This is an important motivation for measuring f_s . We hope to improve significantly the previous measurements made as we are using a sample more than ten times bigger than the one used by Shin-Shan Yu [19]. Another advantage of this analysis is that we are fully reconstructing all our decay channels, reducing the model dependence on determining the p_T of the B hadrons. We also use a lower p_T threshold than that of semileptonic decays, like the ones used in Karen Gibson's analysis [15], due to the significantly lower backgrounds afforded by the full reconstruction approach.

This thesis describes the data reduction, candidate signal selection, and transverse momentum spectrum ratio determination of the four decay channels under investigation. The document is divided in the following way. The Fermilab accelerator complex and the CDF detector are described in Chapter 2, while the skimming of the datasets we used is covered in Chapter 3. Chapter 4 covers how the signal yields are extracted from the data. We discuss how we obtain the shape of the various B -hadron p_T spectra, explain how systematic uncertainties are calculated and state our results in Chapter 5. We conclude with a discussion of the results, a summary and plans for the future.

CHAPTER 2

Experimental Apparatus

The Fermilab Tevatron (Figure 2–1) is currently the highest energy accelerator in the world. The Tevatron ring collides thirty-six counter circulating bunches of protons and antiprotons ($p\bar{p}$). Collisions occur every 396 ns at a center-of-mass energy of 1.96 TeV in two interaction regions along the ring: B0, which is the site of the CDF experiment, and D0, where the DZero experiment is located.



Figure 2–1: Fermilab accelerator complex.

Both the accelerator and the collider detectors underwent major upgrades between 1997 and 2001. The time between collisions (or beam crossings) was decreased from $3.5 \mu\text{s}$ to 396 ns for the current collider. This new collider configuration required extensive detector upgrades at CDF-II to accommodate the shorter bunch

spacings and higher luminosity. We give an overview of the stages of production and acceleration of the proton and antiproton beams in the next section. We then follow with a description of the CDF-II detector, with a focus on the parts of the detector that are relevant for this analysis.

2.1 The Fermilab National Accelerator Complex Laboratory

The Cockcroft-Walton pre-accelerator is the first stage in the acceleration of protons. Inside this device, hydrogen gas is ionized to create H^- ions, which are accelerated to 750 keV of kinetic energy. Next, the H^- ions enter a linear accelerator (Linac), approximately 500 feet long, where they are accelerated to 400 MeV. The acceleration in the Linac is done by a series of “kicks” from RF cavities. The oscillating electric field of the RF cavities groups the ions into bunches. The Booster accepts 400 MeV H^- ions from the Linac, strips the two electrons off, and accelerates the protons to an energy of 8 GeV. The intensity of the proton beam is increased by injecting new protons into the same orbit as those already circulating. Protons are extracted from the Booster into the Main Injector, where the protons are accelerated from 8 GeV to 150 GeV before the injection into the Tevatron. Alternatively, the Main Injector also accelerates protons to 120 GeV, where the protons collide with a nickel target, and produce a wide spectrum of secondary particles, including antiprotons. About 20 antiprotons are produced per one million incident protons. The antiprotons are collected, focused, and then stored in the Accumulator ring. Once a sufficient number of antiprotons are produced, they are sent to the Main Injector and accelerated to 150 GeV. Finally, both the protons and antiprotons are injected into the Tevatron.

The Tevatron is a ring, 6.28 km in circumference, on which the collider experiments are located. It accelerates both protons and antiprotons from 150 GeV to 980 GeV and intersects the two counter circulating beams at the two interaction points on the ring (B0 and D0). We use the term “luminosity” to quantify the beam particle density and the crossing rate. It can be expressed as

$$L = \frac{f N_B N_p N_{\bar{p}}}{2\pi(\sigma_p^2 + \sigma_{\bar{p}}^2)} F\left(\frac{\sigma_l}{\beta^*}\right) \quad (2.1)$$

where f is the revolution frequency, N_B is the number of bunches, $N_{p/\bar{p}}$ are the number of protons/antiprotons per bunch, and $\sigma_{p/\bar{p}}$ are the RMS beam sizes at the interaction point. F is a form factor that corrects for the bunch shape and depends on the ratio of σ_l , the bunch length, to β^* , the beta function, at the interaction point. The beta function is a dimensionless quantity that describes the evolution of the beam width near the Interaction Point (IP).

2.2 The Collider Detector at Fermilab

The Collider Detector at Fermilab (CDF-II) is a multi-purpose, azimuthally symmetric detector, designed to study $p\bar{p}$ collisions at the Tevatron. A solid cutaway view of the detector can be seen in Figure 2–2. The CDF-II detector is described in detail elsewhere [27]. Major components of the CDF-II detector are described briefly here while parts relevant to this analysis are described in more detail in the following subsections. The detector consists of a tracking system inside a 1.4 Tesla (T) magnetic field, electromagnetic and hadronic calorimeters outside of the tracking system, and muon chambers beyond the calorimeters.

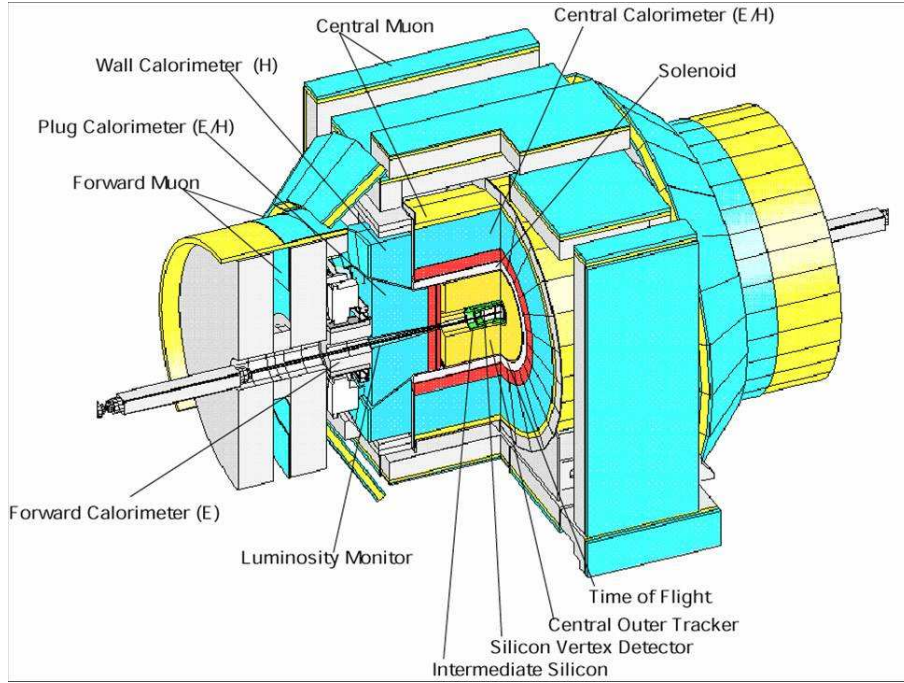


Figure 2–2: Solid-cutaway view of the CDF-II detector.

Because of its barrel-like detector shape, CDF-II uses a right-handed, cylindrical coordinate system (r, ϕ, z) with the origin at the center of the detector and the z -axis along the nominal direction of the proton beam. The y -axis points vertically upward while the x -axis points radially outward from the center of the Tevatron ring. A polar angle, θ , may also be used to describe particle trajectories. An alternate variable often used in place of the polar angle is pseudorapidity (η) defined

$$\eta = -\log \left(\tan \frac{\theta}{2} \right). \quad (2.2)$$

The transverse momentum (p_T) is defined as

$$p_T = p \sin \theta. \tag{2.3}$$

2.3 Tracking Systems

The CDF tracking system is composed of three silicon detector systems and a large volume drift chamber imbedded in a 1.4 T solenoidal magnetic field. A layer of single-sided silicon micro-strips, called Layer 00 (L00) [28], is mounted on the beam pipe, at a radius of 1.7 cm from the beam. L00 is not part of the CDF-II technical design, as it was introduced later as an enhancement to the silicon systems to improve the impact parameter resolution on tracks. L00 is followed by five double-sided layers of silicon sensors, also called SVX-II [29], located at radii between 2.5 and 10.6 cm. Two forward layers of silicon arranged outside of the SVX-II, called the Intermediate Silicon Layers (ISL) [30], constitute the outermost silicon subdetectors systems. The radial extent of the silicon system is from $1.5 \text{ cm} \leq r \leq 28 \text{ cm}$, while the detector extends $\sim 90 \text{ cm}$ along the z -axis, as seen on Figure 2–3.

The silicon systems provide precise position information for the reconstruction of charged particles and decay vertices. The drift chamber occupies a large volume and a large number of channels to provide good pattern recognition and good measurement of the curvature of the charged particles in the magnetic field. Details of each system are described in the sections that follow.

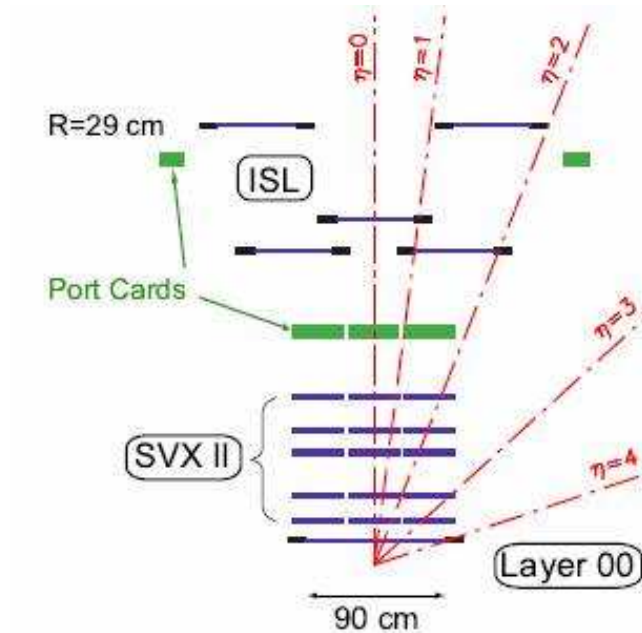


Figure 2–3: Schematic of the CDF Run II silicon detector.

2.3.1 Central Outer Tracker

The Central Outer Tracker (COT) is a cylindrical open-cell drift chamber. The COT provides accurate information in the $r - \phi$ plane for the measurement of transverse momentum, and substantially less accurate information in the $r - z$ plane for the measurement of the z component of the momentum, p_z . This tracking system contains 96 sense wire layers, which are radially grouped into eight “superlayers” as shown on Figure 2–4.

Each superlayer is divided in ϕ into a set of drift cells. Each drift cell contains 13 potential wires interspaced by 12 sense wires, all gold plated tungsten with a diameter of $40 \mu\text{m}$. The wires are sandwiched by two field (cathode) sheets made of $6.35 \mu\text{m}$ thick Mylar with vapor-deposited gold on both sides. Each field sheet is

1/6th West Endplate, Gas Side
 Units: inches [cm]

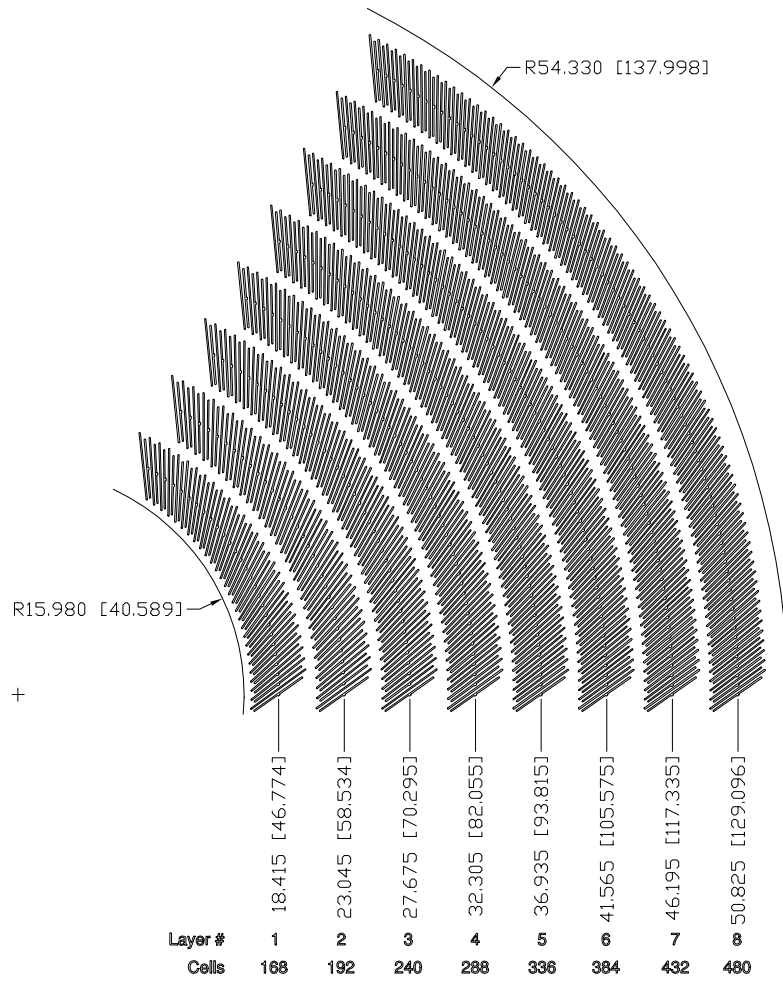


Figure 2-4: Layout of wire planes on a COT endplate.

shared with the neighboring cell. The entire COT contains 2,520 cells and 30,240 sense wires. Each cell is tilted by a Lorentz angle of 35° with respect to the radial direction to compensate for the electron drift created by the magnetic field in which the COT is immersed. A Lorentz angle, also called drift angle, is the angle by which particles moving in an electric field are deflected due to the effect of a magnetic field. Approximately half the wires run along the z direction (axial). The other half are strung at a small angle (2°) with respect to the z direction (stereo) in order to give track information in this same z direction, which is impossible to obtain using axial wires. The active volume of the COT begins at $r=43.4$ cm and extends to $r=132.3$ cm, while covering 310 cm in the z direction. Particles originating from the interaction point that have $|\eta| < 1$ pass through all 8 superlayers of the COT while particles that have $|\eta| < 1.3$ pass through 4 or more superlayers. The COT is filled with an Argon/Ethane gas mixture (50:50).

Signals on the sense wires are read out by the ASDQ (Amplifier, Shaper, Discriminator with charge encoding) chip, which was developed by Bokhari and Newcomer [31]. The ASDQ provides input protection, amplification pulse shaping, baseline restoration discrimination and charge measurement. The analog signal arrives at the ASDQ and the output is a digital pulse. The charge measurement is encoded in the width of the discriminator output pulse, and is used for particle identification by measuring the ionization along the trail of the charged particle (dE/dx). The ASDQ pulse is then sent through ~ 10.5 m of micro-coaxial cable, via repeater cards to Time to Digital Converter (TDC) boards in the collision hall. Hit times are later

processed by pattern recognition (tracking) software to form helical tracks. Using cosmic ray events, the transverse resolution achieved by the COT is measured to be

$$\sigma(p_T)/p_T^2 = 0.0017(\text{GeV}/c)^{-1}. \quad (2.4)$$

2.3.2 Track Reconstruction

Particles moving through a homogeneous solenoidal magnetic field follow helical trajectories. To uniquely parameterize a helix in three dimensions, five parameters are needed. The CDF-II coordinate system chooses three of these parameters to describe a position, and two more to describe the momentum vector at that position. The three parameters describing the position also describe the point of closest approach of the helix to the beam line. These parameters are d_0 , ϕ_0 and z_0 , which are the r , ϕ and z cylindrical coordinates of the point of closest approach of the helix to the beam. The momentum vector is described by the track curvature (C) and the angle of the momentum in the $r - z$ plane ($\cot \theta$). The curvature is signed so that the charge of the particle matches the charge of the curvature. The positively charged tracks curve counterclockwise in the $r - \phi$ plane when looking in the $-z$ direction and the negative charged tracks bend clockwise. The transverse momentum (p_T) is related to C , the magnetic field (B_{mag}) and the charge of the particle in the following way:

$$p_T = Q \cdot \frac{1.49898 \cdot 10^{-4} \cdot B_{mag}}{C}, \quad (2.5)$$

where

$$C = \frac{1}{2Q\rho}. \quad (2.6)$$

C is the curvature, ρ is the radius of the circle made by a track and Q is the sign of the charge of that same track. B_{mag} is measured in Tesla. At any given point of the helix, the track momentum is tangent to the helix. The sign of d_0 is taken to be that of $\hat{p} \times \hat{d} \cdot \hat{z}$, where \hat{p} , \hat{d} and \hat{z} are unit vectors in the direction of p_T , d_0 and z , respectively. For decaying particles, we define the transverse displacement L_{xy}

$$L_{xy} = \vec{d} \cdot \hat{p}_T, \quad (2.7)$$

where \vec{d} is the displacement of the decay vertex in the transverse plane, and \hat{p}_T is the unit vector in the direction of p_T .

2.3.3 Pattern Recognition Algorithms

As explained in the previous sections, charged particles leave small charge depositions as they pass through the tracking system. By following, or “tracking” these depositions, pattern recognition algorithms can reconstruct the charged particle tracks.

The offline track reconstruction begins using only COT information. The first step is to look for a circular path in the axial superlayers of the COT. The algorithm looks for four or more hits in each axial superlayer to form a straight line (segment). The hits on the segment are reconstructed using the time difference between when

the ionization occurs, t_0 (the collision time corrected for the time of flight of the charged particle), and when the signal is picked up by the wire (the leading edge time of the digital pulse from the TDC). The straight-line fit for a segment gives sufficient information to extrapolate rough measurements of curvature and ϕ_0 . Once segments are found, there are two approaches to track finding. One approach is to link together the segments for which the measurements of curvature and ϕ_0 are consistent. The other approach is to improve the curvature and ϕ_0 measurement of a segment reconstructed in superlayer 8 by constraining its circular fit to intersect the beamline, and then adding hits that are consistent with this path. Once a circular path is found in the $r - \phi$ plane, segments and hits in the stereo superlayers are added by their proximity to the circular fit. This results in a three-dimensional track fit. Typically, if one algorithm fails to reconstruct a track, the other will not. This results in a high reconstruction efficiency ($\sim 95\%$) in the COT for tracks that pass through all eight superlayers ($p_T \geq 400$ MeV/c). This efficiency increases to $\sim 98\%$ for tracks with $p_T > 10$ GeV/c. Once a track is reconstructed in the COT, it is extrapolated into the SVX-II. A three-dimensional “road” is formed around the extrapolated track, based on the estimated errors on the track parameters. Starting from the outermost layer, and working inward, silicon clusters found inside the road are added to the track. As a cluster is added, a new track fit is performed, which modifies the error matrix for the track parameters and produces a narrower road. Reducing the width of the road reduces the chance of adding a wrong hit to the track, and reduces computation time. In the first pass of this algorithm, $r - \phi$ clusters are added. In the second pass, clusters with stereo information are added to the track.

2.4 Trigger System

Online triggering systems are necessary because it is physically impossible to store information about every single $p\bar{p}$ collision. The collision rate is ~ 1.7 MHz whereas data can only be stored to tape at a rate of 50 Hz. Also, the total hadronic cross-section (including the elastic, inelastic, and diffractive processes) is about 75 mbarn and the $b\bar{b}$ cross-section is approximately 1000 times smaller, 0.1 mbarn. The CDF-II trigger is designed to be “deadtimeless”. This means that the trigger system has to be quick enough to make a decision for every bunch crossing. Each level of the trigger is given an amount of time to make the decision of accepting or rejecting an event. At the first level (Level 1), a trigger decision is made based only on a subset of the detector, and quick pattern recognition or a simple counting algorithm. The decision time for the Level 1 trigger is about $5.5 \mu\text{s}$ and its rejection factor around 150, giving an event accept rate of 40 kHz. The second level of the trigger (Level 2) does a limited event reconstruction. Its decision time is $20 \mu\text{s}$ and the rejection factor is again around 150, for an accept rate of 300 Hz. The third level of the trigger (Level 3) uses the full detector information to fully reconstruct events in a processor farm. The Level 3 trigger decision time is ~ 1 s and its rejection rate is about 10, resulting in 30 events/sec being accepted and written to tape. The delay necessary to make a trigger decision is achieved by storing detector readout information in a storage pipeline, as shown in Figure 2–5.

A set of requirements that an event has to fulfill at Level 1 (L1), Level 2 (L2) and Level 3 (L3) constitutes a trigger path. Requiring that an event was accepted through a well defined trigger path eliminates volunteer events. A volunteer event

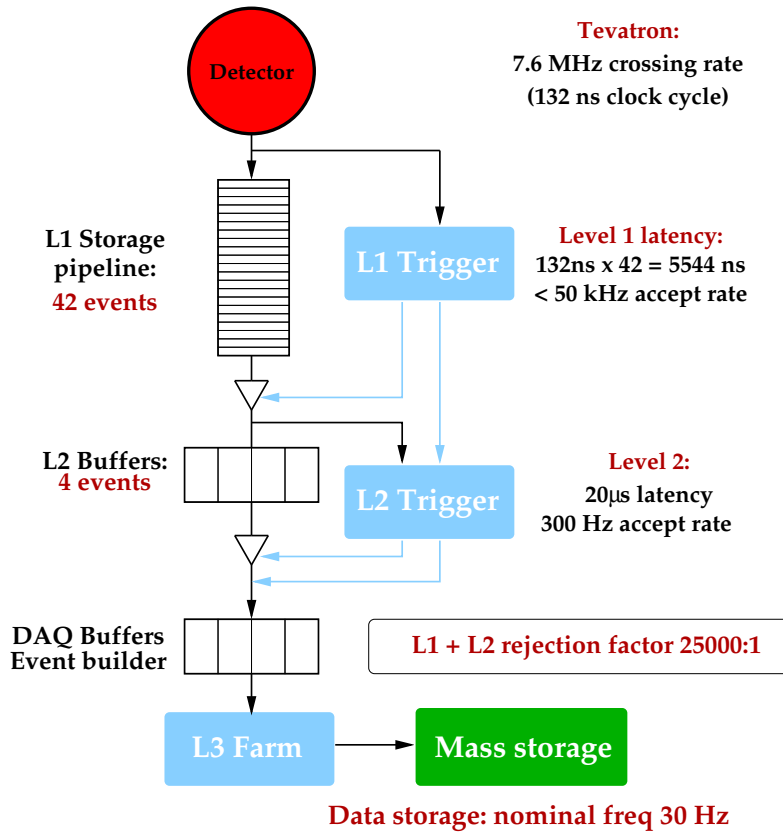


Figure 2-5: Diagram of the CDF-II trigger system.

is an event that passed a higher level trigger, L2 (L3), requirement but that passed a different lower level trigger from another path, L1 (L1, L2). At CDF-II, there are about 100 different trigger paths. The trigger path used for this analysis is one of the B_CHARM trigger paths of the Two Track Trigger (TTT).

The TTT is optimized for finding charm and bottom hadrons that decay into hadronic final states. The strategy of the trigger path is as follows. At Level 1, the eXtremely Fast tracker (XFT) measures the track p_T and angle ϕ . The XFT is a set of custom electronics decoding time information from the drift chamber. By cutting

on p_T , most of the inelastic background will be rejected. The Extrapolation Unit (XTRP) selects an XFT track above a certain p_T threshold and sends a signal to the L1 Track Trigger. The L1 Track Trigger counts the number of tracks from the XTRP; if more than six tracks are found, an automatic “Level 1 accept” is generated. If not, depending on other trigger requirements, the L1 Track Trigger either accepts or rejects the event. If a “L1 accept” is received, the XFT track information is sent to the Level 2 Silicon Vertex Tracker (SVT). At Level 2, the additional time available for reconstruction utilizes the SVX-II information to obtain better impact parameter (d_0) measurements of the tracks. Requiring non-zero impact parameters of tracks will select only tracks that come from the decays of long-lived particles, charm and bottom hadrons.

We choose to reconstruct all decay sequences using the B_CHARM trigger path, in order to cancel the systematic uncertainties associated with the trigger efficiency. The B_CHARM trigger path [32], [33] requires two displaced tracks from the Silicon Vertex Trigger (SVT), and applies cuts on p_T and impact parameter of each track. We select only the ‘Scenario A’ B_CHARM trigger path for the skimming of the datasets described in the next chapter, in order to simplify any subsequent study of efficiency. The cuts at Level 1-3 (L1-3) triggers of the B_CHARM Scenario A trigger path are described below, where L1, L2 are hardware triggers and L3 is a software trigger. The trigger requirements are the following [19]:

Level 1

- a pair of oppositely charged XFT tracks,

- $p_T > 2.04$ GeV/c for each XFT track, where p_T is the momentum of the track in the transverse (xy) plane,
- scalar sum $p_T^1 + p_T^2 > 5.5$ GeV/c,
- $\Delta\phi_0 < 135^\circ$, where ϕ_0 is the azimuthal direction of a track near the beam axis and $\Delta\phi_0$ is $\phi_0^1 - \phi_0^2$ for the pair of tracks.

Level 2

- a pair of oppositely charged SVT tracks,
- each SVT track satisfies:
 - $p_T > 2$ GeV/c,
 - SVT impact parameter (d_0): $120 \mu\text{m} \leq d_0(\text{SVT}) \leq 1000 \mu\text{m}$, where d_0 is the distance measured from the track to the beam axis in the transverse plane,
 - SVT track fit $\chi^2 < 25$,
- scalar sum $p_T^1 + p_T^2 > 5.5$ GeV/c,
- $2^\circ < \Delta\phi_0 < 90^\circ$.

Level 3

- each Level 3 track: $p_T > 2$ GeV/c and $|\eta| < 1.2$,
- scalar sum $p_T^1 + p_T^2 > 5.5$ GeV/c,
- $2^\circ < \Delta\phi_0 < 90^\circ$,
- $L_{xy} \geq 200 \mu\text{m}$, where L_{xy} is the decay length of the two-track vertex with respect to the beam axis,
- $\Delta z_0 < 5$ cm, where z_0 is the z position of the track when closest to the beam axis, in the z direction.

Once the data are selected by the trigger path requirements, the data are written to mass storage (magnetic tape) for subsequent analysis. In the next chapters we describe how the raw data are converted to quantities from which we can reconstruct the B -hadron decays that are the subject of this thesis.

CHAPTER 3

Skimming of the datasets

We will now describe the method used for the skimming of the datasets for this analysis [34]. This was a big part of the analysis as the time required to write the skimming code and do the actual skimming was approximately half the time we took to bring the analysis to the point it is at the time of this writing.

3.1 Trigger and Data Sample

The data used in the skim described here were taken with the CDF detector between February 2002 and January 2007 corresponding to data runs 138425 through 233111 (Table 3–1). Note that all runs are included; no good-run list is applied. Accepting only data from the B hadronic datasets, the above compressed data sample corresponds to 775,237,942 events stored on 35.29 TB of tape. The data are processed using CDF production version 5.3.1 and 6.1.1, and compressed into `xbhd0d`, `xbhd0h` and `xbhd0i` datasets. However, the size of the `xbhd0d` (12.96 TB), `xbhd0h` (9.19 TB) and `xbhd0i` (13.14 TB) datasets presents a problem since we may wish to analyze this data multiple times. We reduce the size of these datasets by applying a set of loose cuts that remove most of the background and keep most of the signal for the four decay sequences used in this thesis. During the skim, we redirect the output into four streams, one for each decay sequence. The combined size of the resulting datasets is 34.39 GB, representing a reduction factor of more than 1000.

Table 3–1: Datasets used in skimming and relevant information.

Dataset	Runs	Data Taking Period	Int. Lum. (pb^{-1})
xbhd0d	138425 to 186598	02/04/02 to 08/22/04	489
xbhd0h	190697 to 203799	12/07/04 to 09/04/05	443
xbhd0i	203819 to 233111	09/05/05 to 01/31/07	943

3.2 Selection Requirements

The skimming code starts looking for tracks that satisfy the cuts listed below, then requires that the resulting track collection contains at least four tracks, that are then ordered in decreasing p_T , since all desired decay sequences have a four-track topology:

- $p_T \geq 0.4$ GeV/ c , to have reconstructible tracks;
- $|\eta| < 1.2$, to select only tracks from the central part of the detector;
- $|d_0| < 0.2$ cm, to eliminate long-lived particles;
- COT stereo hits ≥ 20 , COT axial hits ≥ 20 , a track quality requirement;
- SVX $r - \phi$ hits in different layers ≥ 3 , a track quality requirement;
- $r \geq 140$ cm (COT exit radius cut), requiring tracks to get out of the tracking system.

The code is then separated into four channels, one for each decay sequence. Each event is processed by all four channels and may be written to one or more output streams (one output stream per decay channel). The code from each channel loops over all possible 3-track combinations within a particular event to form a charm particle candidate. Charm candidates are then passed into a fourth loop where a pion is added to form a b candidate. The block of code for a decay sequence contains four nested loops (over selected tracks), one for each final state particle from the

decay. In each loop, the track is assigned a particular mass corresponding to one of the final state particles in the decay. Figure 3–1 shows a block diagram of the skimming algorithm. The particle mass assignments are ordered as follows where the particles expected to appear later in the decay chain are reconstructed first:

- K^-, K^+, π^-, π^+ for the B_s sequence,
- K^+, π^-, π^-, π^+ for both B^0 sequences,
- p, K^-, π^+, π^- for the Λ_b sequence.

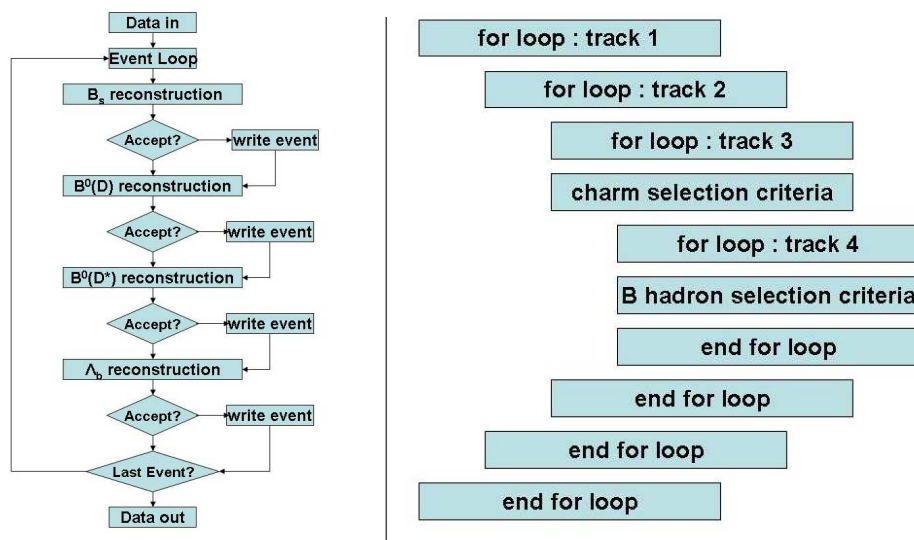


Figure 3–1: Block diagram of the skimming algorithm (left) and a schematic of the B -hadron reconstruction (right).

3.3 Signal Reconstruction

The reconstruction of each decay sequence is described in detail in the following subsections. For each decay sequence, we require that the first two tracks, any

two-different tracks, have opposite charge and that they satisfy the following requirements: $\Delta z_0 \leq 5$ cm and $\Delta R \leq 1$, where $\Delta R = \sqrt{\Delta\phi^2 + \Delta\eta^2}$ and $\Delta\phi$, $\Delta\eta$ are the differences between the two tracks' ϕ and η , respectively.

3.3.1 D_s^+ Reconstruction

We reconstruct the D_s^+ candidates by first looking for the decay $\phi \rightarrow K^+K^-$. We loop over the pair of any two oppositely charged tracks and assign both of them the kaon mass. We impose an upper limit on the raw¹ invariant mass ($\text{raw } M_{KK} \leq 1.05$ GeV/ c^2) of the track pair to eliminate background from Λ and K_S particles. We then add a third track and require that its charge be the same as the first track's. We assign the pion mass to this third track and cut on the raw invariant mass of the newly formed three-track object ($1.876 < \text{raw } M_{KK\pi} < 2.056$ GeV/ c^2). We then perform a three-track kinematic fit using the CTVMFT package developed by Marriner [35]. The invariant mass distributions of the two-track and three-track objects are shown in Figure 3–2. The invariant mass cuts applied on the two-track and three-track objects are chosen to be approximately five standard deviations around the signal peak. These loose requirements are used because we are skimming the data and don't want to eliminate signal candidates. The same procedure is applied to the other modes.

¹ The raw invariant mass uses the (unfitted) track momentum and the assumed particle mass to calculate each particle's four-momentum.

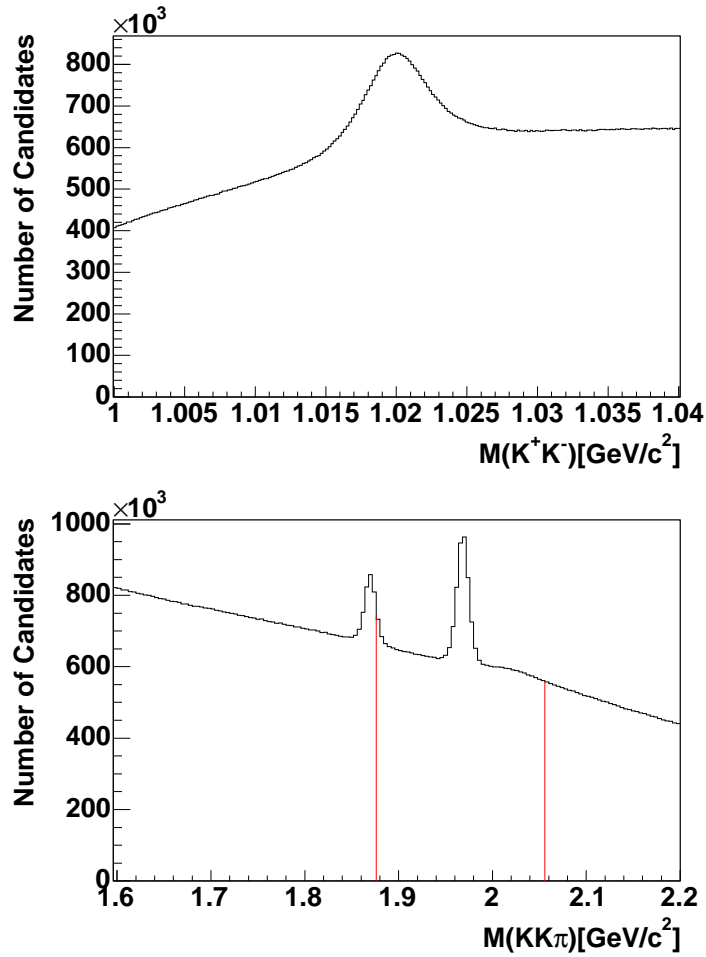


Figure 3–2: $M(KK)$ (top) and $M(KK\pi)$ (bottom) distributions. The red vertical lines represent the cuts applied on the $KK\pi$ invariant mass in the skimming code. The second peak on the $M(KK\pi)$ distribution includes D candidates.

3.3.2 D^+ and Λ_c^+ Reconstruction

We reconstruct the D^+ particles by looping over all possible combinations of three charged tracks. The sum of the three charges has to be either -1 or +1. We require at least one of the first three tracks to be matched to an SVT track. We assign the pion mass to the same-sign charged tracks and the kaon mass to the other track. We then cut on the raw mass of the three-track object ($1.824 < \text{raw } M_{K\pi\pi} < 1.9 \text{ GeV}/c^2$).

For the Λ_c^+ reconstruction, we use the same procedure as D^+ except we assign the proton mass to the higher p_T track of the same-sign charged pair. We also assign the pion mass to the other track of the pair and the kaon mass to the oppositely charged track. Detailed cuts are listed below. The charm invariant mass distributions are shown in Figure 3-3.

- $p_T(p) > p_T(\pi)$,
- $2.216 < \text{raw } M_{pK\pi} < 2.356 \text{ GeV}/c^2$.

3.3.3 D^{*+} Reconstruction

The D^{*+} reconstruction is a bit different since this decay sequence has a different topology (2-2) from the decays previously described. This reconstruction begins by identifying $\bar{D}^0 \rightarrow K^+\pi^-$ candidates. We loop over pairs of two oppositely charged tracks, then assign the kaon mass to the first track, and the π mass to the second and *vice versa*. We require one of the two tracks to be matched to an SVT track and cut on the raw mass of the track pair ($1.3 < \text{raw } M_{K\pi} < 2.5 \text{ GeV}/c^2$). We add a third track then cut on $M_{K\pi\pi}$ ($\text{raw } M_{K\pi\pi} \geq 1.9 \text{ GeV}/c^2$) and on the mass difference ($\text{raw } M_{K\pi\pi} - M_{K\pi} < 0.18 \text{ GeV}/c^2$). Note that the cut on $M_{K\pi\pi}$ is chosen

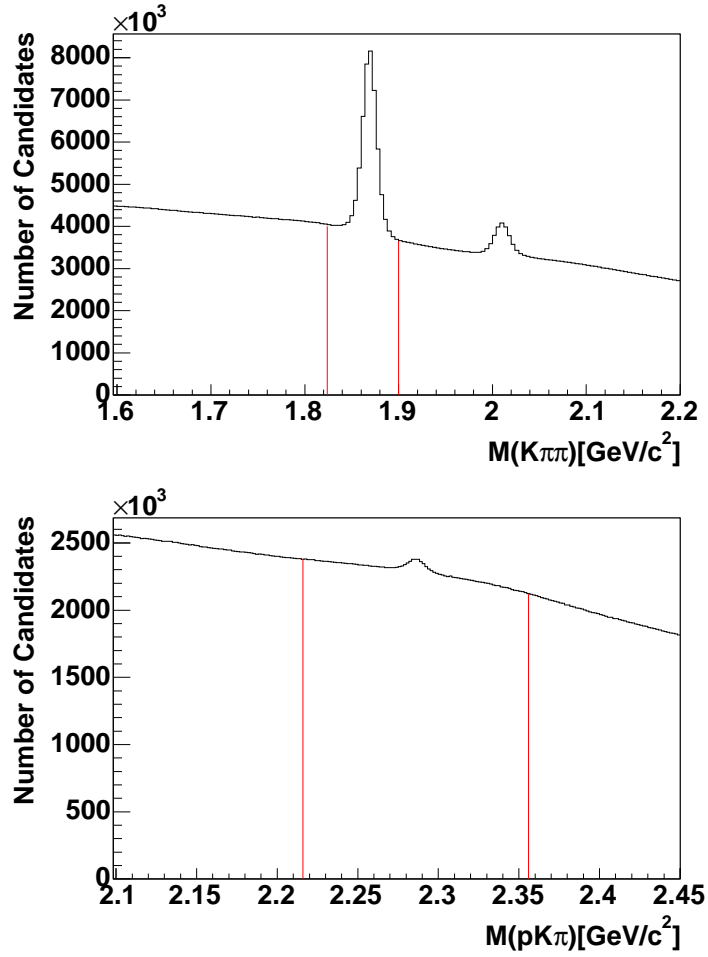


Figure 3–3: $M(K\pi\pi)$ (top) and $M(pK\pi)$ (bottom) distributions. The red vertical lines represent the cuts applied on the invariant masses in the skimming code. The second peak on the $M(K\pi\pi)$ distribution includes D^* candidates.

to accept only events that weren't accepted by the D^+ channel. This complementary cut ensures that no reconstructed B^0 particle is double counted. Again, the invariant mass distributions of the two-track and three-track objects are shown in Figure 3–4.

We also require the following cuts to be satisfied for all decay sequences:

- $p_T(\text{charm candidate}) \geq 4.0 \text{ GeV}/c$,
- three-track kinematic fit probability $\geq 10^{-4}$, where we constrain the three tracks to originate from a common vertex and evaluate the “goodness” of the fit using a reduced χ^2 . This takes into account the number of degrees of freedom (ndf) and gives back a fit probability,
- $L_{xy} \geq 0.02 \text{ cm}$, where L_{xy} is the distance between the primary vertex and the charm vertex.

3.3.4 B Hadron Reconstruction

We add a fourth track to the three tracks already forming the $D_s^-/D^{*-}/D^-/\Lambda_c^+$ candidate to form a B -hadron candidate. We then cut on the raw mass of the four-track object and reconfirm the impact parameter (d_0) requirement of each individual track. We require that the fourth track be matched to an SVT track. Both the matched SVT tracks and the reconstructed tracks are required to pass ‘Scenario A’ cuts of the B-CHARM trigger path listed in Section 2.4.

We then perform a four-track kinematic fit. In the four-track fit, we constrain the tertiary vertex to point to the pion track from the B -hadron decay (1-3 topology) or to the di-pion vertex (2-2 topology). We further constrain the masses of the charm particles (D_s^- , D^- , D^{*-} , Λ_c^+) to the Particle Data Group (PDG) values [36]. To constrain a mass in a particular fit simply means to fix the desired mass to the

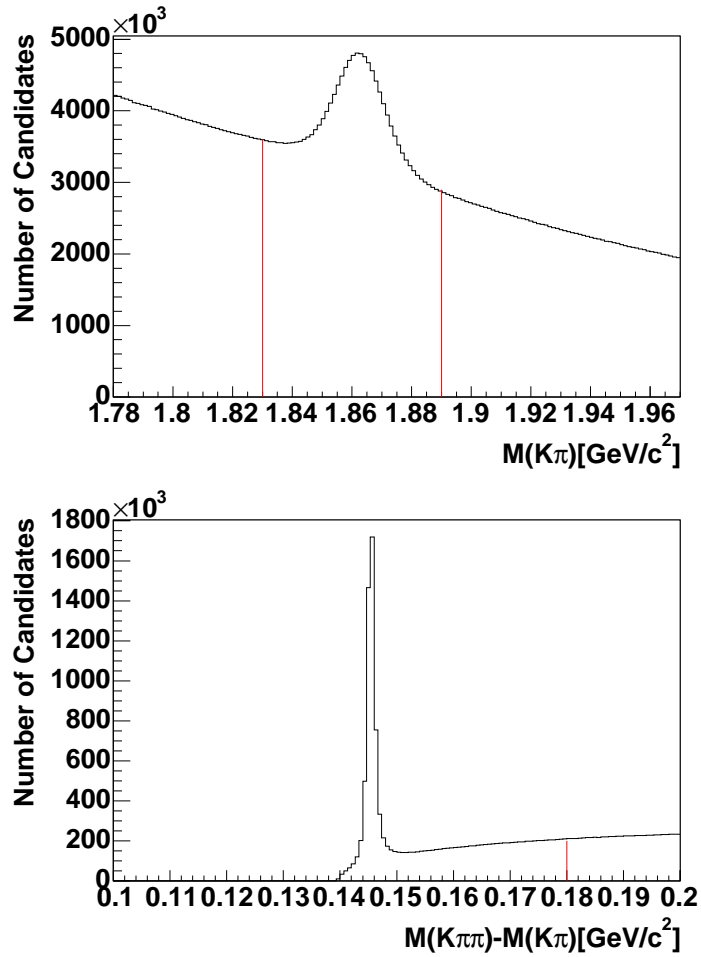


Figure 3–4: $M(K\pi)$ (top) and $M(K\pi\pi) - M(K\pi)$ (bottom) distributions. The red vertical lines represent the cuts applied on the invariant mass (top) and on the mass difference (bottom) in the skimming code.

PDG mass and to vary the other track parameters (such as momenta) within their uncertainties in order to obtain the best kinematic fit. In addition, only for the B^0 candidate reconstructed from the D^{*+} , we impose a mass constraint on the D^0 mass. We also cut on the p_T , fitted mass and L_{xy} of the B candidates. In this situation, L_{xy} is defined as the distance between the primary vertex and secondary vertex. Detailed cuts are listed below:

- $|d_0|(\text{track}) \leq 0.2 \text{ cm}$,
- $4.0 < \text{raw M}(\text{four tracks}) < 8.0 \text{ GeV}/c^2$,
- p_T of four-track object $\geq 6.0 \text{ GeV}/c$,
- four-track kinematic fit probability with mass constraint $\geq 10^{-4}$,
- $4.5 < \text{M}(B \text{ hadron}) < 7.0 \text{ GeV}/c^2$,
- $L_{xy} \geq 0.02 \text{ cm}$, where L_{xy} is the distance between the primary vertex and the B -hadron vertex.

Invariant mass distributions showing the B -hadron signals are shown in Figures 3–5, 3–6, 3–7 and 3–8. The lines on the plots represent fits to extract the B -hadron yields. These fits are described in the next section.

It is interesting to note that the cuts applied in the skimming code are loose enough so that an event can pass the requirements in more than one decay channel. We recorded the overlap between different reconstructed decay sequences and have observed that the biggest one is between the B^0 and the Λ_b channels, where a 9.4% overlap was recorded. The overlap between all the other channels has been observed to be small ($<1\%$).

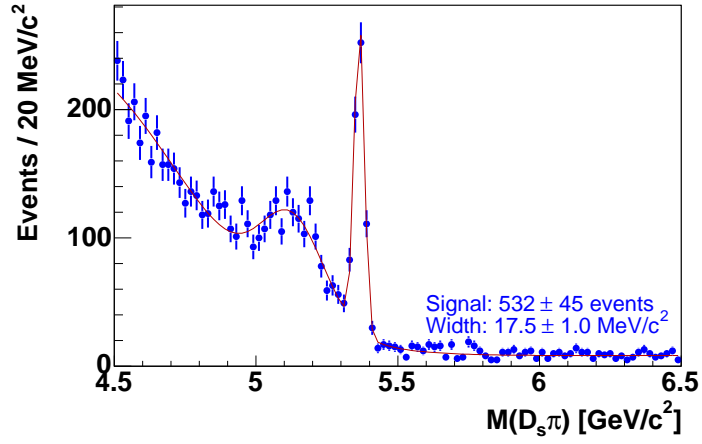


Figure 3-5: $M(D_s\pi)$ distribution. Yield and width obtained from a binned χ^2 fit.

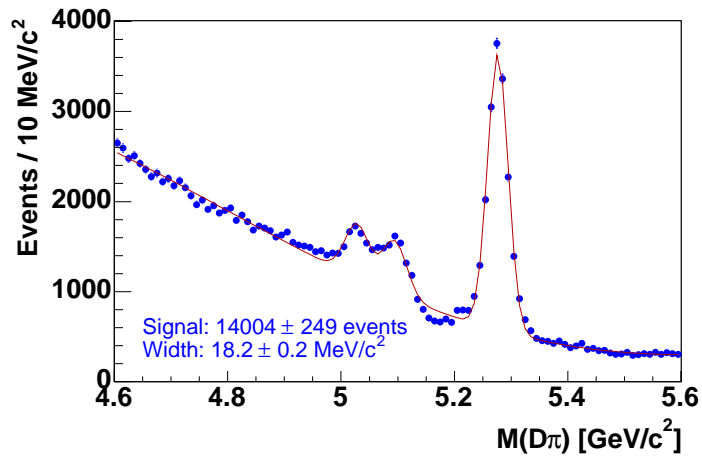


Figure 3-6: $M(D\pi)$ distribution. Yield and width obtained from a binned χ^2 fit.

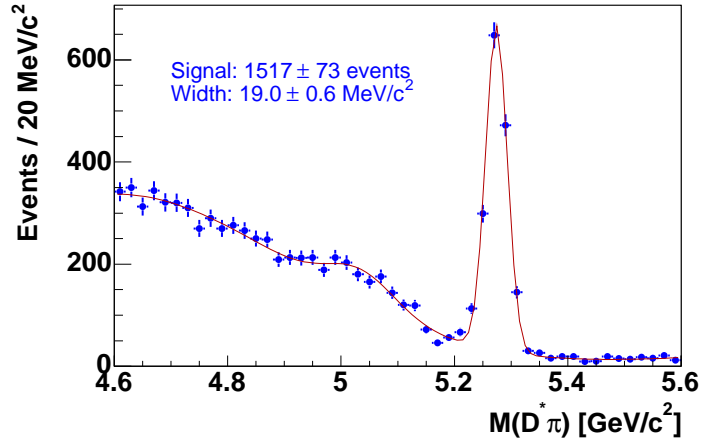


Figure 3–7: $M(D^*\pi)$ distribution. Yield and width obtained from a binned χ^2 fit.

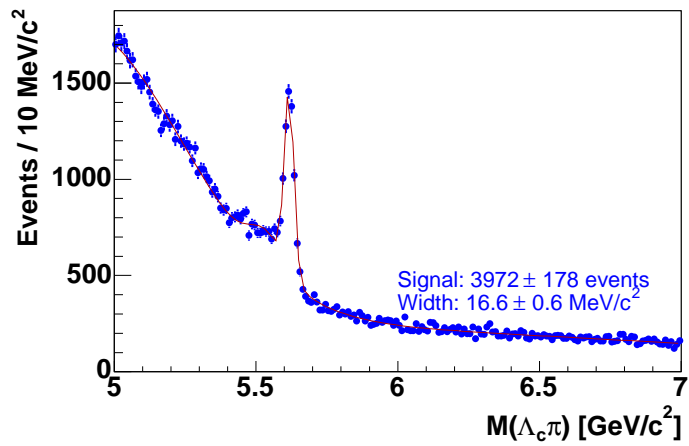


Figure 3–8: $M(\Lambda_c\pi)$ distribution. Yield and width obtained from a binned χ^2 fit.

3.3.5 *B* Hadron Mass Fit

In order to estimate the amount of signal contained in the four datasets resulting from this skim, we fit the *c*-hadron+ π invariant mass distributions using a binned χ^2 technique. In all fits we represent the signal with a single Gaussian and use different functional forms to represent different backgrounds. The high mass region is largely combinatorial (charm particle matched to a random track) and is represented by a linear function. The parameters inputted to these functions were obtained by fitting separately different regions of the invariant mass distributions. For the $D_s\pi$ and $D^*\pi$ distributions, the fit parameters were obtained by fitting the signal with one Gaussian function, the low-side background (mostly composed of partially reconstructed and mis-reconstructed decays) with two Gaussians and the high-side background with a first order polynomial. The $D\pi$ distribution was fitted using a Gaussian for the signal region, a double-Gaussian plus another Gaussian for the low-side background region and a first order polynomial for the high-side background region. For the $\Lambda_c\pi$ distribution, the fit parameters were obtained by fitting the signal with two Gaussians, the low-side background with one Gaussian and the high-side background with a first order polynomial. These fits are very “rough” and are made only to give us an idea of the amount of signal we have for each decay mode. Better fits describing the *B*-hadron invariant mass spectra, hence giving us more precise yield estimates, are described in the next chapter. All fits are shown in Figures 3–5, 3–6, 3–7 and 3–8 with their respective yields and widths. The uncertainties indicated are statistical only.

3.3.6 Data Quality

Not all the runs contained in the skimmed datasets are useful for this analysis. For example, some part of the detector crucial in reconstructing B hadrons might have been turned off during some runs due to technical problems. In order to only keep runs in which we reconstruct candidates relevant for this analysis, we checked the quality of the data reconstructed during the skim. This simple procedure was applied to identify problematic runs for further study.

We used the mean and width of the $D^+ \rightarrow K^- \pi^+ \pi^+$ signal to identify problems as a function of run number. The D^+ is the largest signal we obtain during the skim and we use this signal to check data quality. For a given run, if the mean or width of the D^+ peak in the $K\pi\pi$ mass spectrum is more than three standard deviations (σ) away from the value obtained from most runs, we flag that run for further study. Figure 3–9 shows the two distributions and the cuts applied. This figure also shows a distribution of D^+ yield versus run number since the CDF offline machinery doesn't allow us to get the prescaled luminosity for all the runs. From 3520 runs, three were found to be outside the 3σ range for the mean distribution, compared to 32 for the width distribution. Out of these “problematic” runs, only two, common to both distributions, were due to detector related problems (SVT turned off during those runs). For all the remaining problematic runs (30) we found that the fit for the D^+ signal failed due to insufficient data in the $K\pi\pi$ mass distribution.

3.4 Summary

Using the skimming procedure described in this chapter, we reduced the `xbhd0d`, `xbhd0h` and `xbhd0i` datasets by a factor of 1000 and reconstructed the following fully

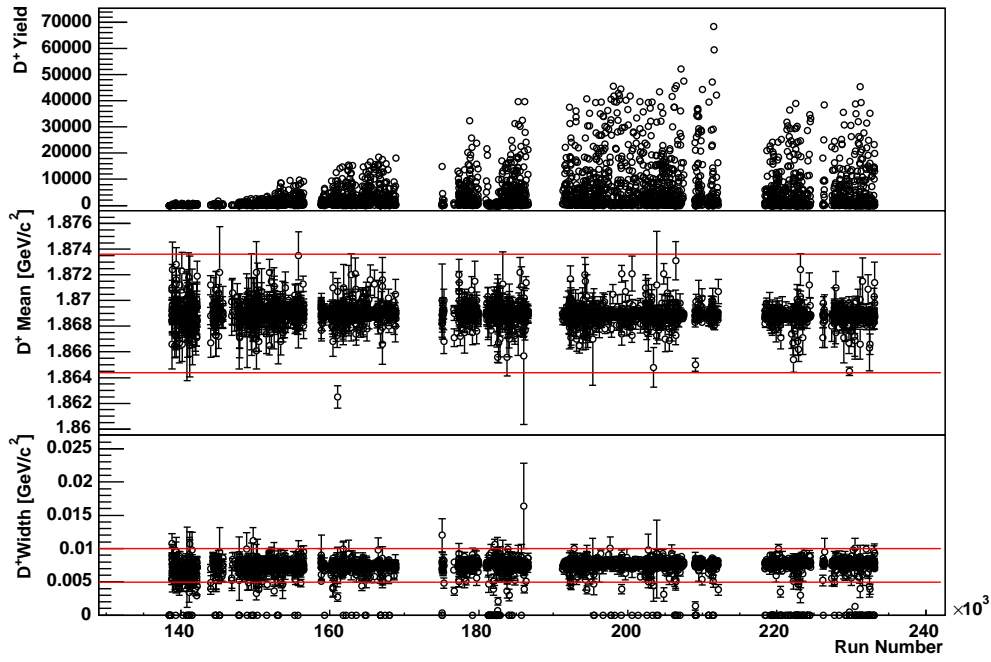


Figure 3-9: D^+ yield, $M(D)$ mean and width vs run number. (Top) D^+ yield vs run number. (Middle) $M(D)$ mean vs run number. (Bottom) $M(D)$ width vs run number. In the bottom two distributions, the two red horizontal lines indicate the three sigma region around the mean value.

hadronic modes: $B_s^0 \rightarrow D_s^- \pi^+$, where $D_s^- \rightarrow \phi \pi^-$, $\phi \rightarrow K^+ K^-$; $B^0 \rightarrow D^- \pi^+$, where $D^- \rightarrow K^+ \pi^- \pi^-$; $B^0 \rightarrow D^{*(2010)-} \pi^+$, where $D^{*-} \rightarrow \bar{D}^0 \pi^-$, $\bar{D}^0 \rightarrow K^+ \pi^-$; and $\Lambda_b^0 \rightarrow \Lambda_c^+ \pi^-$, where $\Lambda_c^+ \rightarrow p K^- \pi^+$. In 1.9 fb^{-1} of data, we reconstructed 532 ± 45 $B_s^0 \rightarrow D_s^- \pi^+$, 14004 ± 249 $B^0 \rightarrow D^- \pi^+$, 1517 ± 73 $B^0 \rightarrow D^{*-} \pi^+$ and 3972 ± 178 $\Lambda_b^0 \rightarrow \Lambda_c^+ \pi^-$ candidate decays.

CHAPTER 4

Signal Optimization and Yields

Now that we have reduced our datasets and made sure that we have a well defined signal for each of the decay modes we want to reconstruct, we can optimize our signal and find appropriate functional forms to describe the B -hadron invariant mass distributions, accounting for the relevant background sources.

From the reduced datasets we reconstruct our signals:

- $B_s^0 \rightarrow D_s^- \pi^+$, where $D_s^- \rightarrow \phi \pi^-$, $\phi \rightarrow K^+ K^-$,
- $B^0 \rightarrow D^- \pi^+$, where $D^- \rightarrow K^+ \pi^- \pi^-$,
- $B^0 \rightarrow D^{*-} \pi^+$, where $D^{*-} \rightarrow \bar{D}^0 \pi^-$, $\bar{D}^0 \rightarrow K^+ \pi^-$,
- $\Lambda_b^0 \rightarrow \Lambda_c^+ \pi^-$, where $\Lambda_c^+ \rightarrow p K^- \pi^+$.

Additional, or more restrictive, selection is applied to the data to improve the significance of the signals. Significance is defined as $S/\sqrt{S+B}$, where S and B are the number of signal and background events in the signal region of our data, respectively.

This additional selection is the following:

- $|d_0(B \text{ hadron})| < 0.01 \text{ cm}$,
- $L_{xy}(B \text{ hadron}) \geq 0.04 \text{ cm}$,
- B -hadron kinematic fit probability $\geq 10^{-3}$.

The cuts on the B -hadron impact parameter and kinematic fit probability are based on cuts from [37]. An optimization of these cuts will be made for our specific analysis in future work. The L_{xy} cut is actually optimized to obtain the best significance for

our signals. To optimize this cut, we look at the significance of the signal versus possible L_{xy} cut values. We determine the optimized selection, found to be 0.04 cm, as the lowest L_{xy} value for which the significance is at its maximum. We use only data to do the optimization. We can do so because we have a well established signal and we are not looking for a new particle or a new decay mode. Otherwise, this could bias our sample. S and B are obtained by fitting the signal region with a Gaussian function and an exponential function and by taking the integral under these functions. The number of events under the Gaussian gives us S , while the integral under the exponential returns B . The selection for each B hadron was optimized independently. We found the optimized selection for each particle similar to that of the B_s . We use the B_s optimized selection for all reconstructed B hadrons. We can see plots of the significance of the signal versus L_{xy} for all decay channels in Figures 4–1.

4.1 B Hadron Invariant Mass Fit

Each B -hadron invariant mass spectrum is fitted using a combination of functions that describe the signal and the various background contributions. The functional forms for the signal and background sources are determined empirically from the mass spectra by breaking up each spectrum into regions that are dominated by a single process. Processes that add components to each mass spectrum are the following: partially reconstructed decays, mis-reconstructed decays, signal and combinatorial background. Partially reconstructed decays are decays for which one or more particles are not reconstructed by our analysis code. For example, we do not reconstruct neutral particles in this analysis, so a decay that has one such particle

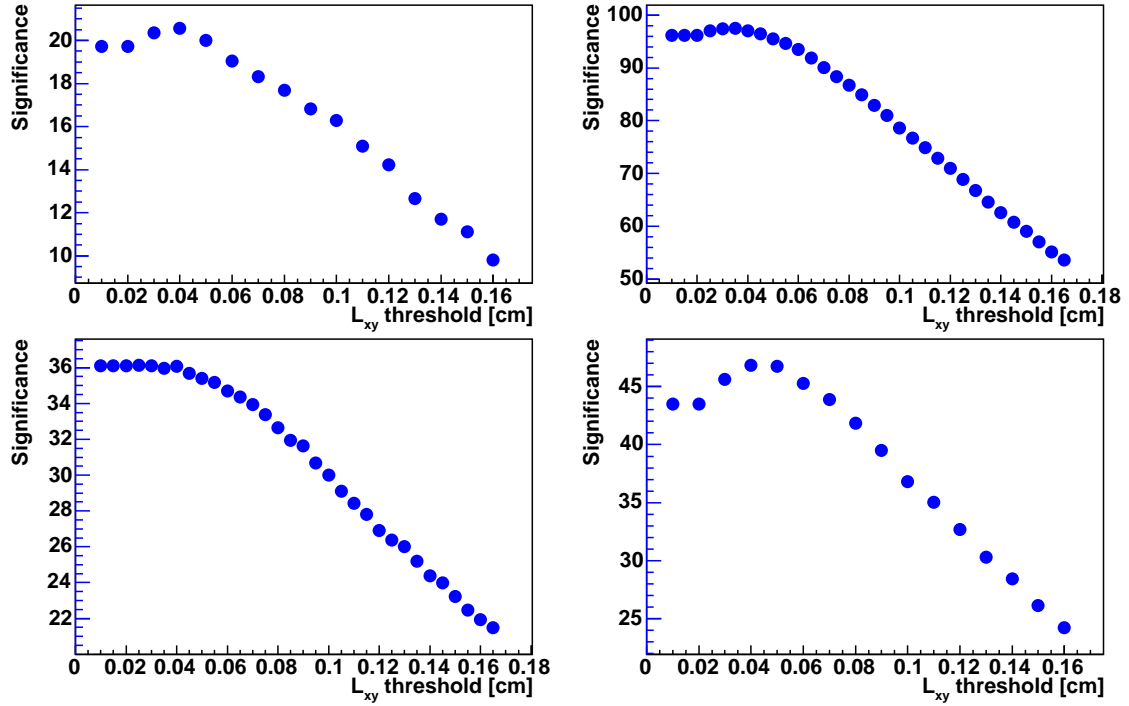


Figure 4-1: Significance versus L_{xy} distribution for $B_s^0 \rightarrow D_s^- \pi^+$ (top left), $B^0 \rightarrow D^- \pi^+$ (top right), $B^0 \rightarrow D^{*-} \pi^+$ (bottom left) and $\Lambda_b^0 \rightarrow \Lambda_c^+ \pi^-$ (bottom right). The L_{xy} values are in centimeters.

in its final state will always be partially reconstructed. Mis-reconstructed decays are decays for which one or more final state tracks are assigned wrong masses, thus reconstructed as particles other than what they should be. The invariant mass distribution resulting from such track combinations is shifted from the invariant mass of the signal. The combinatorial background is a type of background caused by the inclusion in the invariant mass spectrum of wrong mass-assignment combinations between those particles that compose the signal-mode final state. We determine each functional form by fitting the data in a region for a single functional form describing the dominant process for that region, after subtraction of the other processes that contribute to that region. After the shape for each component is determined, the combined function is used to fit each individual mass spectrum. A description of each component of the combined function for every decay mode follows.

4.1.1 $B_s^0 \rightarrow D_s^- \pi^+$ Fit

The combined fitting function for the $B_s^0 \rightarrow D_s^- \pi^+$ invariant mass distribution has four different contributions apart from the signal function. The function used to describe the signal is the same for all decay channels except for $B^0 \rightarrow D^- \pi^+$:

$$S(m) = N_S \cdot \left[G(m, \mu_S, \sigma_0) + R_1 \cdot G(m, \mu_S, \sigma_1) \right], \quad (4.1)$$

where the first Gaussian (G) describes the signal peak and the second Gaussian (resolution Gaussian) approximates the non-Gaussian tails in our mass resolution. N_S and R_1 are normalization variables describing the amount of signal and the relative amount of the long tails, respectively. The mean of the signal peak is μ_S ,

while σ_0 and σ_1 are the widths of the narrow component of the signal Gaussian and the resolution Gaussian, respectively. R_1 and σ_1 are fixed in the global fit using data. To do so, we subtract all the background contributions from the invariant mass distribution until we have only the signal peak and a flat line as background. Then, we fit the signal peak using $S(m)$ and extract R_1 and σ_1 . The following background contributions are observed [38]: Cabibbo suppressed decays $B_s \rightarrow D_s^- K^+$, misreconstructed decays $B_s \rightarrow D_s^{*-} \pi^+$ and $B_s \rightarrow D_s^- \rho^+$, partially reconstructed decays $B_s \rightarrow D_s^- X$ and combinatorial background.

1. $B_s \rightarrow D_s^- K^+$: Cabibbo suppressed decays. We use generator level Monte Carlo (MC) to extract the shape of the distribution. A small description of how we generate our MC can be found in the next chapter. We reconstruct the kaon as a pion in the MC sample and smear the mass of the B hadron by the width of the narrow component of the signal Gaussian in the data to account for detector effects. We find that the shape of the Cabibbo suppressed decays in the MC is modeled by a skewed Gaussian (SG), which can be described by the following functional form:

$$f(x) = 2\phi(x) \otimes \Phi(\alpha x), \quad (4.2)$$

with

$$\phi(x) = \frac{e^{-\frac{x^2}{2}}}{\sqrt{2\pi}} \quad (4.3)$$

and

$$\Phi(\alpha x) = \int_{-\infty}^{\alpha x} \phi(t) dt. \quad (4.4)$$

The normalization should be determined by scaling the normalization of the signal Gaussian by the ratio of branching ratios

$BR(B_s \rightarrow D_s^- K^+)/BR(B_s \rightarrow D_s^- \pi^+)$. Since no measurement of these branching ratios has been performed, we use the analogous ratio

$BR(B^0 \rightarrow D^- K^+)/BR(B^0 \rightarrow D^- \pi^+)$. We do so because the D^+ and D_s^+ mesons have the same total angular momentum and are expected to behave similarly. The Cabibbo suppressed decays are described by the function $C(m)$:

$$C(m) = N_C \cdot SG(m, \mu_{shift}, \sigma_C, s_C), \quad (4.5)$$

where

$$N_C = N_S \cdot \frac{BR(B^0 \rightarrow D^- K^+)}{BR(B^0 \rightarrow D^- \pi^+)} \quad (4.6)$$

and

$$\mu_{shift} = \mu_C \cdot \frac{\mu_S}{m(B_s)_{PDG}}. \quad (4.7)$$

The mean (μ_C), the width (σ_C) and the skewness (s_C) of the skewed Gaussian are extracted from the MC, while N_C , the normalization of the skewed Gaussian, is determined from the normalization of the narrow component of the signal Gaussian. We shift the mean of the skewed Gaussian by the ratio of the mean of the reconstructed B_s hadron from data and the B_s mass obtained from the Particle Data Group (PDG) [36] to account for reconstruction efficiency. This shifted mean is represented by the variable μ_{shift} .

2. $B_s \rightarrow D_s^{*-} \pi^+$ and $B_s \rightarrow D_s^- \rho^+$: mis-reconstructed decays. These decays produce a peak in the $D_s \pi$ invariant mass distribution around 5.15 GeV/ c^2 and the shape is modeled by a single Gaussian:

$$R(m) = N_R \cdot G(m, \mu_R, \sigma_R), \quad (4.8)$$

where N_R , μ_R and σ_R are the normalization, mean and width of the Gaussian.

3. $B_s \rightarrow D_s^- X$: Partially reconstructed decays. The shape of the background composed of the partially reconstructed decays $B_s \rightarrow D_s^- X$ (low side) is modeled by a simple linear function:

$$L(m) = \gamma_0 + \gamma_1 \cdot m, \quad (4.9)$$

where γ_0 is the y -intercept and γ_1 the slope of the line.

4. combinatorial: The combinatorial background is modeled by a linear function similar to the one used for the low side background.

$$H(m) = \gamma_2 + \gamma_3 \cdot m, \quad (4.10)$$

where γ_2 is the y -intercept and γ_3 the slope of the line.

All floating parameters obtained from the fit can be found in Table 4-1, while the fixed parameters extracted from MC or data are in Table 4-2. The $D_s\pi$ invariant mass plot with the binned χ^2 fit is shown in Figure 4-2. We obtain a fit probability of 90.0% and a chi squared per degree of freedom (χ^2/ndf) of 71.5/88 from the fit. After subtracting the different background contributions we obtain

$$N_{B_s \rightarrow D_s^- \pi^+} = 473 \pm 42.$$

4.1.2 $B^0 \rightarrow D^- \pi^+$ Fit

We use a function derived in [38] to describe the $D\pi$ invariant mass spectrum. The different contributions to the background come from the following decays: Cabibbo suppressed decays $B^0 \rightarrow D^- K^+$, mis-reconstructed decays $B^0 \rightarrow D^{*-} \pi^+$ and $B^0 \rightarrow D^{*-} \rho^+$, partially reconstructed decays $B^0 \rightarrow D^- X$ and combinatorial background. We use generator level MC to fix some of the parameters of the fitting function. A different function is used to describe the signal for this mode as it agrees better with the data. This may be because of the quality of the reconstruction of the B^0 meson or simply because we have more data for this particular decay channel. Three Gaussians are used to describe the signal peak and the resolution effects:

Table 4-1: $B_s \rightarrow D_s^- \pi^+$ mass spectrum floating fit parameters.

Parameter	Fit value
γ_2	5.1 ± 0.9
γ_3	-0.70 ± 0.15
γ_0	464 ± 28
γ_1	-88 ± 6
N_R	7.31 ± 0.97
μ_R	5.158 ± 0.006
σ_R	0.094 ± 0.007
N_S	3.9 ± 0.2
μ_S	5.366 ± 0.001
σ_0	0.017 ± 0.001

Table 4-2: $B_s \rightarrow D_s^- \pi^+$ mass spectrum fixed fit parameters.

Parameter	Meaning	Fit value
μ_C	mean of $B_s \rightarrow D_s^- K^+$ [GeV/ c^2]	5.3560 ± 0.0004
σ_C	width of $B_s \rightarrow D_s^- K^+$ [GeV/ c^2]	0.0337 ± 0.0002
s_C	skewness	-14.4 ± 0.4
R_1	fraction of resolution Gaussian	0.19 ± 0.18
σ_1	width of resolution Gaussian [GeV/ c^2]	0.057 ± 0.036

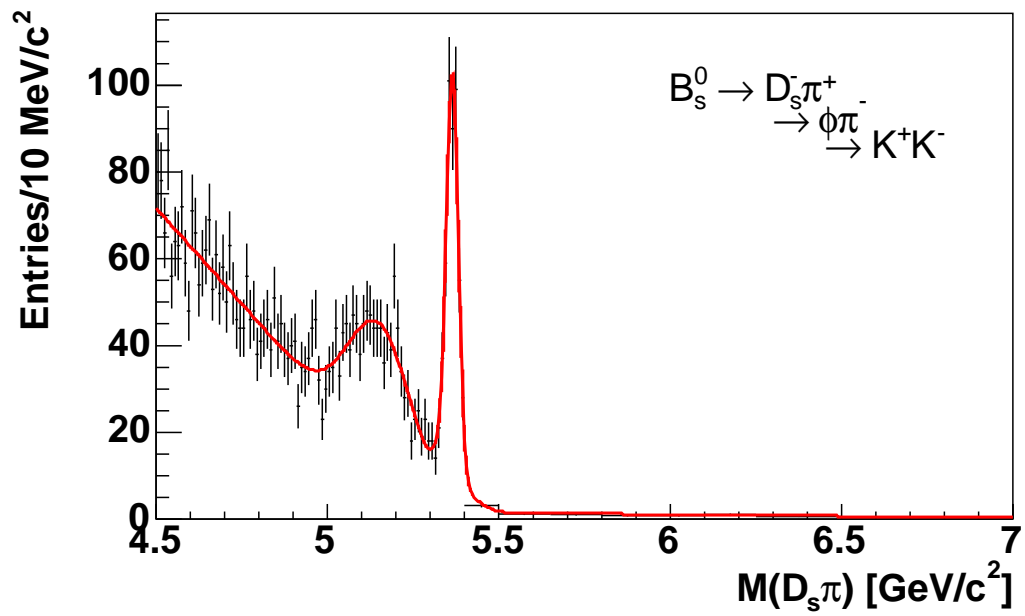


Figure 4–2: $D_s\pi$ invariant mass fit. We do a χ^2 fit using the fitting function described in the text and obtain a fit probability of 90.0% and χ^2/ndf of 71.5/88.

$$S(m) = N_S \cdot \left[G(m, \mu_S, \sigma_0) + R_1 \cdot G(m, \mu_S, \sigma_1) + R_2 \cdot G(m, \mu_S, \sigma_2) \right]. \quad (4.11)$$

N_S , R_1 and R_2 are normalization variables similar to those found in equation 4.1, μ_S is the mean of the signal peak, while σ_0 , σ_1 and σ_2 are the widths of the narrow component of the signal Gaussian and of the Gaussians describing the non-Gaussian tails in our mass resolution, respectively.

1. $B^0 \rightarrow D^- K^+$: Cabibbo suppressed decays. We use generator level MC to extract the shape of the distribution. The method used is the same as described in section 4.1.1. We find that the shape of the Cabibbo suppressed decays is modeled by a skewed Gaussian. The normalization is determined by scaling the normalization of the narrow component of the signal Gaussian by the ratio of branching ratios $BR(B^0 \rightarrow D^- K^+)/BR(B^0 \rightarrow D^- \pi^+)$ [36]:

$$C(m) = N_C \cdot SG(m, \mu_{shift}, \sigma_C, s_C), \quad (4.12)$$

where

$$N_C = N_S \cdot \frac{BR(B^0 \rightarrow D^- K^+)}{BR(B^0 \rightarrow D^- \pi^+)} \quad (4.13)$$

and

$$\mu_{shift} = \mu_C \cdot \frac{\mu_S}{m(B^0)_{PDG}}. \quad (4.14)$$

The variables used to describe this background contribution are defined in section 4.1.1.

2. $B^0 \rightarrow D^- \rho^+$ and $B^0 \rightarrow D^{*-} \pi^+$: these mis-reconstructed decays are included in the same fitting function. The $B^0 \rightarrow D^- \rho^+$ decay forms a continuously rising background that cuts off smoothly and is modeled by a decaying exponential convoluted with a Gaussian, sometimes referred to as a lifetime function [19]. The two horns below the signal peak (see Figure 4-3) are a consequence of the $B^0 \rightarrow D^{*-} \pi^+$ decay, where $D^{*-} \rightarrow D^- \pi^0$. The missing energy of the π^0 shifts the mass of the reconstructed B^0 , while the two horn structure is caused by the polarization of the D^{*-} in the decay. The shape is modeled by a double Gaussian and combined with the lifetime function describing the $B^0 \rightarrow D^- \rho^+$ decay:

$$P(m) = N_P \cdot \left[(1 - f_H) \cdot \exp(m, \tau_{pol}) \otimes G(m, \mu_{pol}, \sigma_{pol}) + f_H \cdot (0.5 \cdot G(m, \mu_{pol} - \nu_{pol} - \delta_{pol}, \sigma_H) + 0.5 \cdot G(m, \mu_{pol} - \nu_{pol} + \delta_{pol}, \sigma_H)) \right]. \quad (4.15)$$

The exact form of the lifetime function can be found in [39]. The zero point of the lifetime function is μ_{pol} , ν_{pol} is the offset of the mid point between the two horns from the lifetime function and δ_{pol} is half the distance between the two

horns. The lifetime is τ_{pol} , the mean and the resolution of the lifetime function are μ_{pol} and σ_{pol} , respectively, while f_H is the fraction of events in both horns and σ_H is the width of both horns. We assume that the width σ_H is the same for both horns.

3. $B^0 \rightarrow D^- X$: Partially reconstructed decays. The shape of the background composed of the partially reconstructed decays $B^0 \rightarrow D^- X$ is modeled by a simple linear function:

$$L(m) = \gamma_0 + \gamma_1 \cdot m, \quad (4.16)$$

where γ_0 is the y -intercept and γ_1 the slope of the line.

4. combinatorial: The combinatorial background is described by an exponential function:

$$CB(m) = \exp(\gamma_2 + \gamma_3 \cdot m), \quad (4.17)$$

where e^{γ_2} is the y -intercept and γ_3 describes the slope of the exponential.

All floating parameters obtained from the fit can be found in Table 4-3, while the fixed parameters extracted from MC or data are in Table 4-4. The $D\pi$ invariant mass plot with the binned χ^2 fit is shown in Figure 4-3. We obtain a fit probability of 0.79% and a χ^2/ndf of 289.5/234 from the fit. This low fit probability is acceptable since we only wish to have a good understanding of the different backgrounds contributing to the signal region of the invariant mass distribution. The ultimate goal is to obtain

the appropriate yield of B^0 mesons and we think that this global fit describes the invariant mass distribution well enough. After subtracting the different background contributions we obtain

$$N_{B^0 \rightarrow D^- \pi^+} = 15206 \pm 203.$$

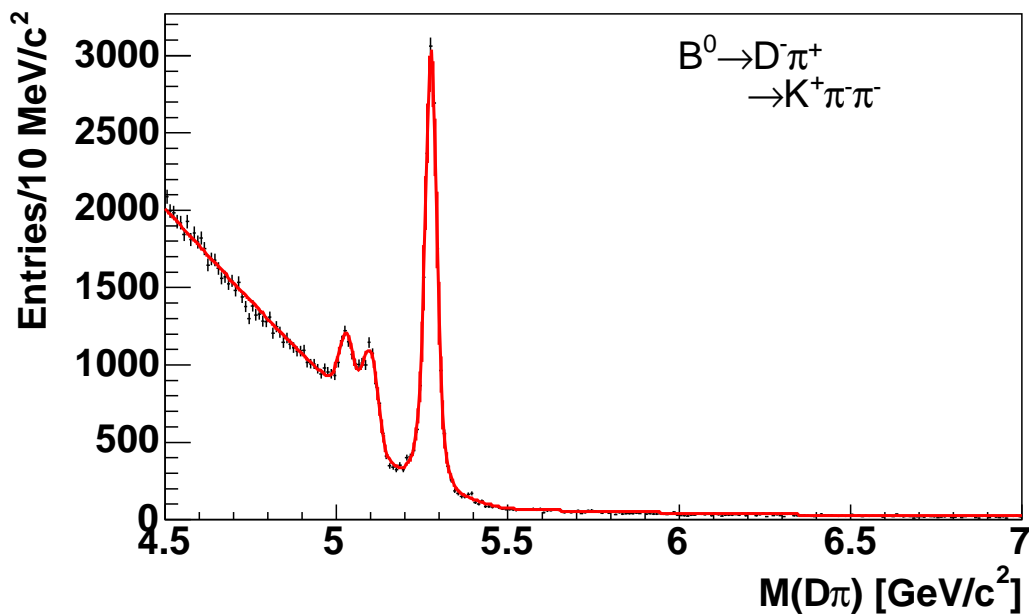


Figure 4-3: $D\pi$ invariant mass fit. We do a χ^2 fit using the fitting function described in the text and obtain a fit probability of 0.79% and χ^2/ndf of 289.5/234.

4.1.3 $B^0 \rightarrow D^{*-} \pi^+$ Fit

The background contributing to the $D^* \pi$ invariant mass distribution can be listed as follows: Cabibbo suppressed decays $B^0 \rightarrow D^{*-} K^+$, mis-reconstructed decays $B^0 \rightarrow D^{*-} \rho^+$, partially reconstructed decays $B^0 \rightarrow D^{*-} X$ and combinatorial background.

Table 4-3: $B^0 \rightarrow D^- \pi^+$ mass spectrum floating fit parameters.

Parameter	Fit value
γ_0	12780 ± 128
γ_1	-2436 ± 25
γ_2	9.2 ± 0.2
γ_3	-0.92 ± 0.04
N_P	10.7 ± 0.4
μ_{pol}	5.129 ± 0.003
$\frac{\tilde{I}_H}{10}$	0.039 ± 0.003
σ_H	0.0210 ± 0.0009
ν_{pol}	0.066 ± 0.004
N_S	84 ± 9
μ_S	5.2769 ± 0.0002
σ_0	0.0150 ± 0.0006
R_1	0.38 ± 0.06
σ_1	0.096 ± 0.007
R_2	0.51 ± 0.16
σ_2	0.029 ± 0.003

Table 4-4: $B^0 \rightarrow D^- \pi^+$ mass spectrum fixed fit parameters.

Parameter	Meaning	Fit value
τ_{pol}	lifetime of $D\rho$ background [c^2/GeV]	0.324 ± 0.008
σ_{pol}	width of $D\rho$ background [c^2/GeV]	0.011 ± 0.002
δ_{pol}	distance between the two horns [GeV/c^2]	0.03366 ± 0.00011
μ_C	mean of $B^0 \rightarrow D^- K^+$ [GeV/c^2]	5.26574 ± 0.00009
σ_C	width of $B^0 \rightarrow D^- K^+$ [GeV/c^2]	0.0341 ± 0.0002
s_C	skewness	-17.7 ± 0.4

1. $B^0 \rightarrow D^{*-}K^+$: Cabibbo suppressed decays. We use generator level MC to extract the shape of the distribution. The method used is the same as described in section 4.1.1. We find that the shape of the Cabibbo suppressed decays is modeled by a skewed Gaussian. The normalization is determined by scaling the normalization of the narrow component of the signal Gaussian by the ratio of branching ratios $BR(B^0 \rightarrow D^{*-}K^+)/BR(B^0 \rightarrow D^{*-}\pi^+)$:

$$C(m) = N_C \cdot SG(m, \mu_{shift}, \sigma_C, s_C), \quad (4.18)$$

where

$$N_C = N_S \cdot \frac{BR(B^0 \rightarrow D^{*-}K^+)}{BR(B^0 \rightarrow D^{*-}\pi^+)} \quad (4.19)$$

and

$$\mu_{shift} = \mu_C \cdot \frac{\mu_S}{m(B^0)_{PDG}}. \quad (4.20)$$

The variables used to describe this background contribution are defined in section 4.1.1.

2. $B^0 \rightarrow D^{*-}\rho^+$ and $B^0 \rightarrow D^{*-}X$: these decays are included in the same fitting function, as it fits our data well. The shape is modeled by the product of a square root function with a step-down function:

$$T(m) = N_T \cdot \sqrt{M_{off} - m} \cdot \left(1 - \frac{1}{1 + e^{(\mu_T - m)/\sigma_0}}\right), \quad (4.21)$$

where M_{off} is where the square root function goes to zero, μ_T is the free parameter of the step-down function and σ_0 is the width of the narrow component of the signal Gaussian.

3. combinatorial: The combinatorial background is described by a linear function:

$$CB(m) = \gamma_0 + \gamma_1 \cdot m, \quad (4.22)$$

where γ_0 is the y -intercept and γ_1 the slope of the line.

All floating parameters obtained from the fit can be found in Table 4–5, while the fixed parameters extracted from MC or data are in Table 4–6. The $D^*\pi$ invariant mass plot with the binned χ^2 fit is shown in Figure 4–4. We obtain a fit probability of 13.2% and a χ^2/ndf of 101.8/87 from the fit. After subtracting the different background contributions we obtain

$$N_{B^0 \rightarrow D^*-\pi^+} = 1483 \pm 45.$$

4.1.4 $\Lambda_b^0 \rightarrow \Lambda_c^+\pi^-$ Fit

We use parts of the function derived in [19] for the fit of the $\Lambda_b^0 \rightarrow \Lambda_c^+\pi^-$ data. We do not use the entire function since we have approximately an order of magnitude more data than was used in [19] and are therefore more sensitive to more subtle background effects. The different background contributions to the

Table 4-5: $B^0 \rightarrow D^{*-}\pi^+$ mass spectrum floating fit parameters.

Parameter	Fit value
γ_0	5.37 ± 1.02
γ_1	-0.70 ± 0.16
N_T	177 ± 3
M_{off}	5.199 ± 0.006
μ_T	5.164 ± 0.006
N_S	11.7 ± 0.3
μ_S	5.275 ± 0.001
σ_0	0.0169 ± 0.0005

Table 4-6: $B^0 \rightarrow D^{*-}\pi^+$ mass spectrum fixed fit parameters.

Parameter	Meaning	Fit value
μ_C	mean of $B^0 \rightarrow D^{*-}K^+$ [GeV/ c^2]	5.2614 ± 0.0002
σ_C	width of $B^0 \rightarrow D^{*-}K^+$ [GeV/ c^2]	0.0394 ± 0.0003
s_C	skewness	-15.8 ± 0.6
R_1	fraction of resolution Gaussian	0.2191 ± 0.0897
σ_1	width of resolution Gaussian [GeV/ c^2]	0.0397 ± 0.0059

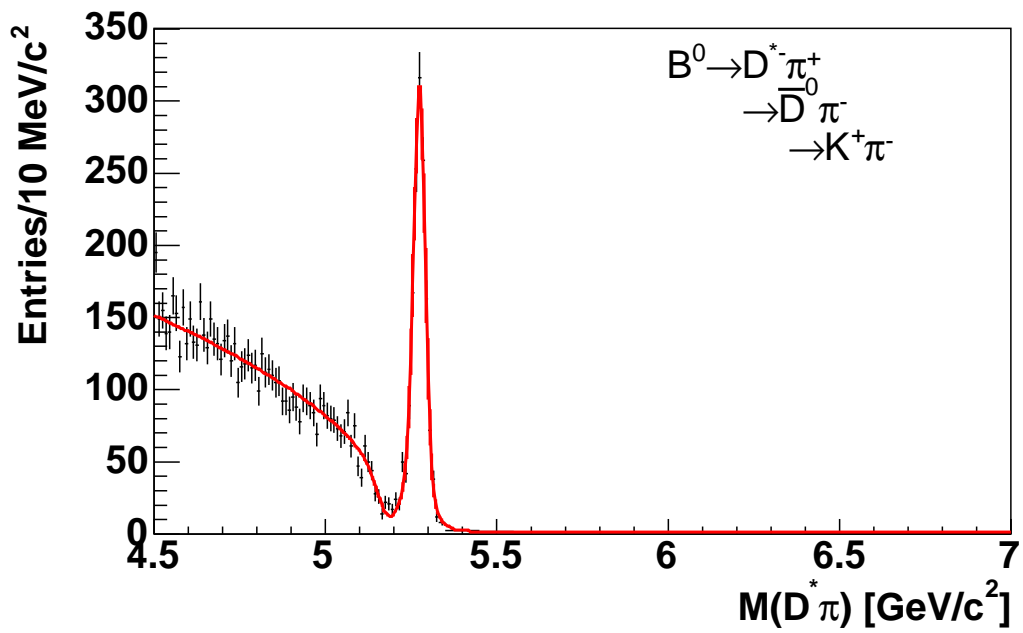


Figure 4–4: $D^* \pi$ invariant mass fit. We do a χ^2 fit using the fitting function described in the text and obtain a fit probability of 13.2% and χ^2/ndf of 101.8/87.

invariant mass spectrum are the following: Cabibbo suppressed decays $\Lambda_b^0 \rightarrow \Lambda_c^+ K^-$, four prong mis-identified B mesons, partially reconstructed decays $\Lambda_b^0 \rightarrow \Lambda_c^+ X$ and combinatorial background.

1. $\Lambda_b^0 \rightarrow \Lambda_c^+ K^-$: Cabibbo suppressed decays. We use generator level MC to extract the shape of the distribution. The method used is the same as described in section 4.1.1. We find that the shape of the Cabibbo suppressed decay is modeled by a skewed Gaussian. We scale by the normalization of the narrow component of the signal Gaussian in a slightly different way for this decay mode for two reasons. First, there are no previous measurements of the branching ratios $\Lambda_b^0 \rightarrow \Lambda_c^+ K^-$ and $\Lambda_b^0 \rightarrow \Lambda_c^+ \pi^-$. Second, the angular momentum of the Λ_b is 1/2 which allows for both S and P waves ($L = 0$ and $L = 1$, respectively) to contribute to the decay. The function describing the Cabibbo suppressed decays is

$$C(m) = N_C \cdot SG(m, \mu_{shift}, \sigma_C, s_C), \quad (4.23)$$

where

$$N_C = N_S \cdot \frac{BR(B^0 \rightarrow D^- K^+) + BR(B^0 \rightarrow D^{*-} K^+)}{BR(B^0 \rightarrow D^- \pi^+) + BR(B^0 \rightarrow D^{*-} \pi^+)} \quad (4.24)$$

and

$$\mu_{shift} = \mu_C \cdot \frac{\mu_S}{m(\Lambda(b)^0)_{PDG}}. \quad (4.25)$$

The variables used to describe this background contribution are defined in section 4.1.1.

2. mis-identified four-prong B mesons: this background is composed of B -hadron decays with a fully reconstructed four-track final state where one or more tracks are mis-reconstructed. The decays that form this background have a similar final state to the signal and thus produce a distinct peak to the left of the signal Gaussian. We model this background using the sum of two Gaussians and a Landau function (L) [40]:

$$B_{4P}(m) = N_{4P} \cdot \left[f_g \cdot G(m, \mu_{bpg}, \sigma_{bpg}) + (1 - f_g) \cdot L(m, \mu_{bpg} + \nu_L, \sigma_L) \right], \quad (4.26)$$

where f_g , μ_{bpg} (μ_{4P}) and σ_{bpg} (σ_{4P}) are the fraction, the mean and the width of the second (first) Gaussian, while ν_L , σ_L and N_{4P} are the distance between the Landau peak and the Gaussian peak, the width of the Landau function and the normalization, respectively. All the parameters, except for N_{4P} , are extracted from data and fixed for the fit. To do so, we temporarily apply a cut on the transverse displacement of the charm-hadron vertex relative to the B -hadron vertex, $L_{xy} > 1$ mm, to eliminate our Λ_b signal and only keep the background coming from the mis-reconstructed B mesons. Applying this

selection preferentially removes Λ_b signal because of the short lifetime of the Λ_c^+ baryon ($\sim 60\mu m$) relative to that of D mesons ($\sim 300\mu m$). We then fit the low side ($[4.8,5.1]$ GeV/c^2) and the high side ($[5.9,7.0]$ GeV/c^2) of the $\Lambda_c\pi$ invariant mass spectrum with straight lines and subtract from it the associated contributions. We fit the resulting shape with the B_{4P} function plus a Gaussian and fix the resulting parameters in the global fitting function. Note that the $L_{xy} > 1$ mm cut is not applied to obtain our final results. It is only used to obtain a parameterization for this particular background source. We use a Gaussian with the B_{4P} function because the data tells us there is another contribution to the background in the form of a small bump with a mean between 5.25 and 5.30 GeV/c^2 . We do not know which decay contributes to this background and it is not important for this analysis since the bump doesn't extend under the signal peak. We add this Gaussian only to have a better agreement between the global fitting function and our data. The normalization, mean and width of the Gaussian are named N_{g1} , μ_{g1} and σ_{g1} , respectively, for bookkeeping purposes. N_{g1} is allowed to float in the global fit while μ_{g1} and σ_{g1} are fixed.

3. $\Lambda_b^0 \rightarrow \Lambda_c^+ X$: Partially reconstructed decays. The shape of this background is modeled using the product of a step-down function with the sum of an exponential function and bifurcated Gaussian (B_F):

$$O_B(m) = N_{ob} \cdot \left[\exp(m) + f_{bg} \cdot B_F \left(m, \mu_{obg}, \sigma_{obg}^L, \sigma_{obg}^R \right) \right] \times \left(1 - \frac{1}{1 + e^{(\mu_{ob} - m)/a_0^{ob}}} \right), \quad (4.27)$$

where f_{bg} , μ_{obg} , σ_{obg}^L and σ_{obg}^R are the fraction, mean, left width and right width of the bifurcated Gaussian. N_{ob} is the normalization, and μ_{ob} and a_0^{ob} are the parameters for the step-down function. We use this complicated function because we know from other analyses that it describes well this particular background and because the use of simpler functions with fewer parameters yielded poorer results. The $\exp(m)$ function is defined the following way when the slope of the exponential, $p_0 \neq 0$:

$$\exp(m) = p_0 \cdot \frac{e^{-p_0 \cdot M_{\text{mid}}}}{e^{-p_0 \cdot M_{\text{min}}} - e^{-p_0 \cdot M_{\text{max}}}} \cdot e^{-p_0 \cdot (m - M_{\text{mid}})}, \quad (4.28)$$

and when $p_0 = 0$,

$$\exp(m) = \frac{1}{M_{\text{max}} - M_{\text{min}}}, \quad (4.29)$$

where M_{max} and M_{min} specify the mass window: $4.8 < M_{\Lambda_c \pi} < 7.0 \text{ GeV}/c^2$ and M_{mid} is the average of M_{max} and M_{min} . All the parameters, except for N_{ob} and f_{bg} , are obtained from [19].

4. combinatorial: The combinatorial background is described by an exponential function:

$$CB(m) = \exp(\gamma_2 + \gamma_3 \cdot m), \quad (4.30)$$

where e^{γ_2} is the y -intercept and γ_3 describes the slope of the exponential.

All floating parameters obtained from the fit can be found in Table 4-7, while the fixed parameters extracted from MC or data are in Table 4-8. The $\Lambda_c\pi$ invariant mass plot with the binned χ^2 fit is shown in Figure 4-5. We obtain a fit probability of 0.48% and a χ^2/ndf of 265.8/209 from the fit. The low fit probability can be explained by the poor choice of function to describe the invariant mass region going from 5.4 to 5.55 GeV/c^2 . This function has now been modified by adding a second Gaussian and gives us much better results for the global fit (fit probability $\sim 1\%$). After subtracting the different background contributions we obtain

$$N_{\Lambda_b \rightarrow \Lambda_c^+ \pi^-} = 4444 \pm 297.$$

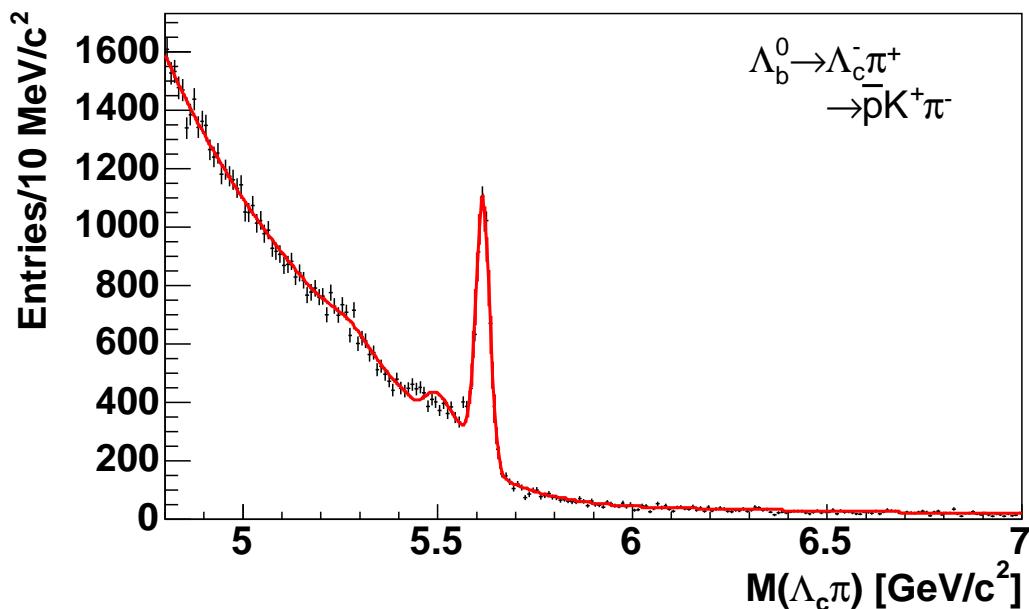


Figure 4-5: $\Lambda_c\pi$ invariant mass fit. We do a χ^2 fit using the fitting function described in the text and obtain a fit probability of 0.48% and χ^2/ndf of 265.8/209.

Table 4-7: $\Lambda_b^0 \rightarrow \Lambda_c^+ \pi^-$ mass spectrum floating fit parameters.

Parameter	Fit value
γ_0	8.9 \pm 0.5
γ_1	-0.88 \pm 0.08
N_{ob}	611 \pm 14
f_{bg}	0.50 \pm 0.07
N_{4P}	42 \pm 2
N_{g1}	5.7 \pm 1.6
N_S	37.6 \pm 0.8
μ_S	5.6174 \pm 0.0004
σ_0	0.0175 \pm 0.0004
R	0.36 \pm 0.06
σ_1	0.15 \pm 0.02

Table 4-8: $\Lambda_b^0 \rightarrow \Lambda_c^+ \pi^-$ mass spectrum fixed fit parameters.

Parameter	Meaning	Fit value
p_0	slope of the exponential, $O_B(m)$	2.180
μ_{obg}	mean of the bifurcated Gaussian [GeV/ c^2], $O_B(m)$	5.598
σ_{obg}^R	right width of the bifurcated Gaussian [GeV/ c^2], $O_B(m)$	4.800
σ_{obg}^L	left width of the bifurcated Gaussian [GeV/ c^2], $O_B(m)$	10.0
a_0^{ob}	slope of the step-down function, $O_B(m)$	0.079
μ_{ob}	mean of the step-down function [GeV/ c^2], $O_B(m)$	5.436
μ_{g1}	mean of the Gaussian, bump	5.28 \pm 0.01
σ_{g1}	sigma of the Gaussian, bump	0.049 \pm 0.013
f_g	fraction of the Gaussian, $B_{4P}(m)$	0.51 \pm 0.08
μ_{bpg}	mean of the Gaussian, $B_{4P}(m)$	5.47 \pm 0.02
σ_{bpg}	width of the Gaussian, $B_{4P}(m)$	0.088 \pm 0.016
ν_L	distance between the Landau peak and the Gaussian peak	0.047 \pm 0.024
σ_L	width of Landau, $B_{4P}(m)$	0.030 \pm 0.003
μ_C	mean of $\Lambda_b^0 \rightarrow \Lambda_c^+ K^-$ [GeV/ c^2]	5.6259 \pm 0.0001
σ_C	width of $\Lambda_b^0 \rightarrow \Lambda_c^+ K^-$ [GeV/ c^2]	0.0313 \pm 0.0002
s_C	skewness	-15.1 \pm 0.4

CHAPTER 5

Results

We have reconstructed signals for the B^0 , B_s and Λ_b decay modes from 1.9 fb^{-1} of $p\bar{p}$ collision data. In the last chapter we obtained a functional description of the various components of the invariant mass spectra. Now we are in a position to obtain the shape of the p_T spectrum for each particle. In this chapter, we describe how the p_T spectrum for each particle is obtained and evaluate the uncertainties associated with each spectrum. Finally we compare the p_T spectra of the particles with that of the B^0 .

5.1 Extracting the p_T spectra

We obtain the p_T spectrum of each B -hadron signal by subtracting the measured p_T spectrum for each background source from the p_T distribution in the signal region. The amount of each background source's p_T spectrum to subtract is estimated from the functional forms determined in the previous chapter projected into the signal region. We can do so because the correlations between the p_T spectra from different regions of the invariant mass spectrum are negligible. We illustrate this technique by showing how we obtain the B_s hadron p_T spectrum and then explain the differences in obtaining the B -hadron spectra for the other modes. It is important to mention that all uncertainties are propagated on a bin-by-bin basis using the following rule when subtracting the p_T spectra from one another:

$$\Delta a = \sqrt{(\Delta b)^2 + (c\Delta N)^2 + (N\Delta c)^2}, \quad (5.1)$$

where $a = b - Nc$, b is the content of one p_T bin in the signal region, N is the normalization factor and c is the background contributing to the signal region for the same p_T bin.

5.1.1 $B_s^0 \rightarrow D_s^- \pi^+$ p_T spectrum

We show the different contributions to the $D_s\pi$ invariant mass fit in Figure 5-1. We number the regions, from which we extract the p_T spectra of the various background contributions and of the signal, from 1 to 4. Region 1 is defined from 4.5 to 4.8 GeV/c^2 and is defined to be the region where the partially reconstructed (PR) decays $B_s \rightarrow D_s^- X$ are dominant. Region 2 is where mis-reconstructed (MR) decays $B_s \rightarrow D_s^{*-} \pi^+$ and $B_s \rightarrow D_s^- \rho^+$ are dominant and is defined from 4.9 to 5.25 GeV/c^2 . From the $D_s\pi$ invariant mass fit, we obtained a width for the narrow component of the signal (SR) Gaussian of $\sim 17 \text{ MeV}/c^2$ so we define the signal region (Region 3) from 5.3 to 5.45 GeV/c^2 , approximately 10σ . The region where random D_s -track combinations (CB) is dominant is labeled 4 and is taken from 6.0 to 7.0 GeV/c^2 . The raw p_T spectrum from each region is shown in Figure 5-2.

We extract the p_T spectra of the different background contributions by taking the raw spectrum for a specific region and by subtracting all the contributions coming from decays that are not dominant for this region. Note that we do not subtract the p_T spectrum associated with the Cabibbo suppressed decays from the signal region as the shapes of this spectrum and of the signal p_T spectrum are the same. We

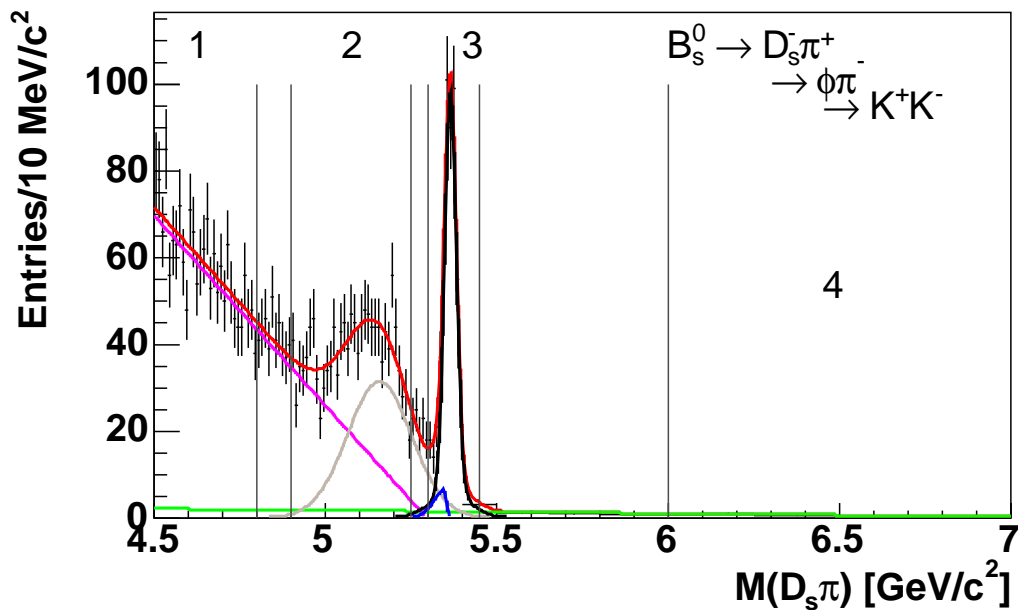


Figure 5–1: $D_s\pi$ invariant mass fit. The components of the fitting function, described in the previous chapter, are shown on the plot while the numbered regions used to extract the p_T spectra of the different background contributions are delimited by the vertical lines: partially reconstructed decays (1), mis-reconstructed decays (2), signal and Cabibbo suppressed decays (3) and random D_s -track combinations or combinatorial background (4).

need to be careful to do the subtractions in the right order as the p_T spectrum for region 4 is the only spectrum that doesn't need to be tampered with. Since only combinatorial background is present in region 4, we can safely assume that $p_T(\text{CB}) = p_T(4)$.

Going in order, we obtained the p_T spectrum from the partially reconstructed decays by doing the following subtraction:

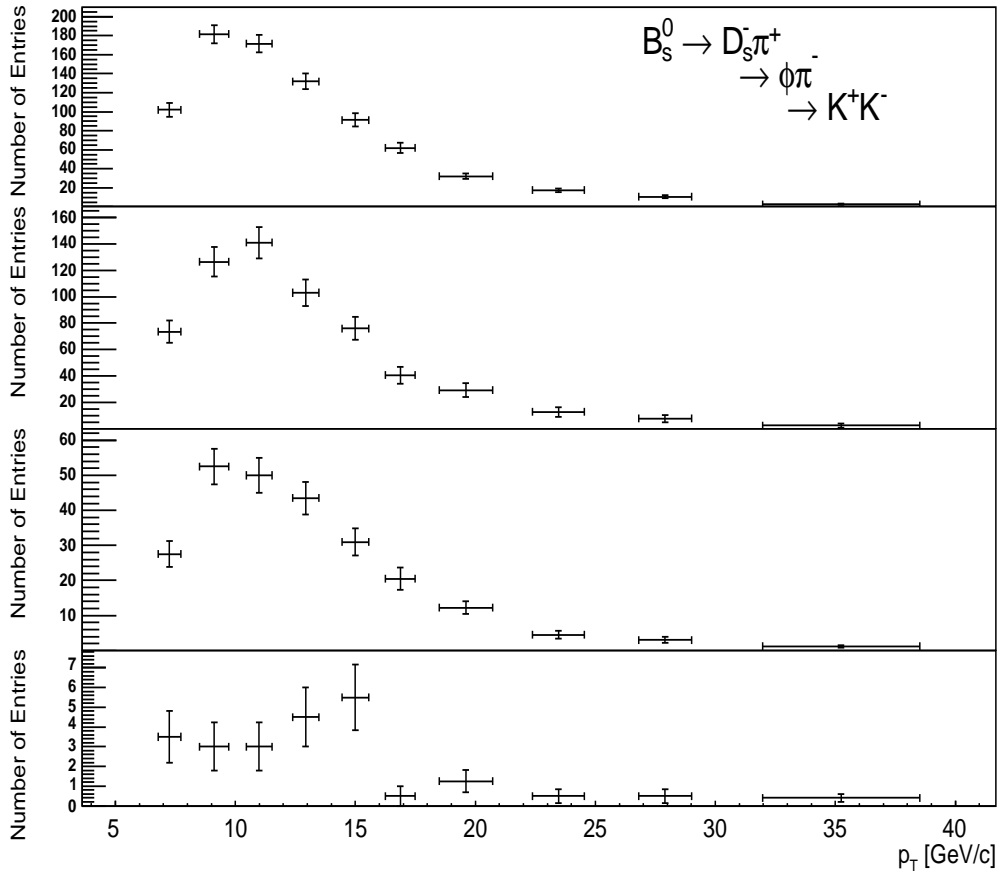


Figure 5-2: Raw p_T spectra for the invariant mass regions 1 (top) to 4 (bottom) in the $B_s^0 \rightarrow D_s^- \pi^+$ mode.

$$p_T(PR) = p_T(1) - k_{41} \cdot p_T(4), \quad (5.2)$$

where $p_T(PR)$, $p_T(1)$ and $p_T(4)$ are the p_T distributions for the PR decays, region 1 and region 4, respectively. The other parameter, k_{41} is a normalization factor defined by the ratio N_{41}/N_4 , where N_{41} is the number of events coming from the CB (region 4) in region 1 and N_4 is the number of events in region 4. The p_T spectrum for the PR decays can be seen in Figure 5–3.

Similarly, the p_T spectra for the mis-reconstructed decays and for the B -hadron signal are obtained from equations 5.3 and 5.4, respectively:

$$p_T(MR) = p_T(2) - k_{42} \cdot p_T(4) - k_{12} \cdot p_T(PR) \quad (5.3)$$

$$p_T(SR) = p_T(3) - k_{43} \cdot p_T(4) - k_{13} \cdot p_T(PR) - k_{23} \cdot p_T(MR). \quad (5.4)$$

The parameters k_{ij} refer to the amount of background coming from region i extrapolated into region j . The same convention will be used throughout this chapter. All the “k” factors can be found in Table 5–1 while the p_T spectra for the MR decays and for the signal can be seen in Figures 5–4 and 5–5, respectively. We can see that, for this mode, the PR decays don’t contribute to the signal region so this reduces the uncertainty on $p_T(SR)$.

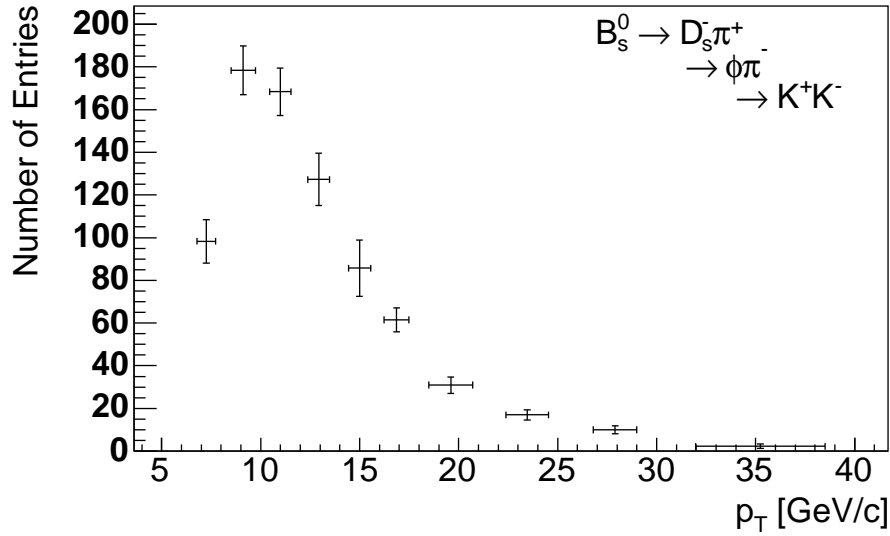


Figure 5-3: p_T spectrum for the partially reconstructed (PR) decays in the $B_s^0 \rightarrow D_s^- \pi^+$ mode. The points are positioned horizontally using the average transverse momentum in each bin.

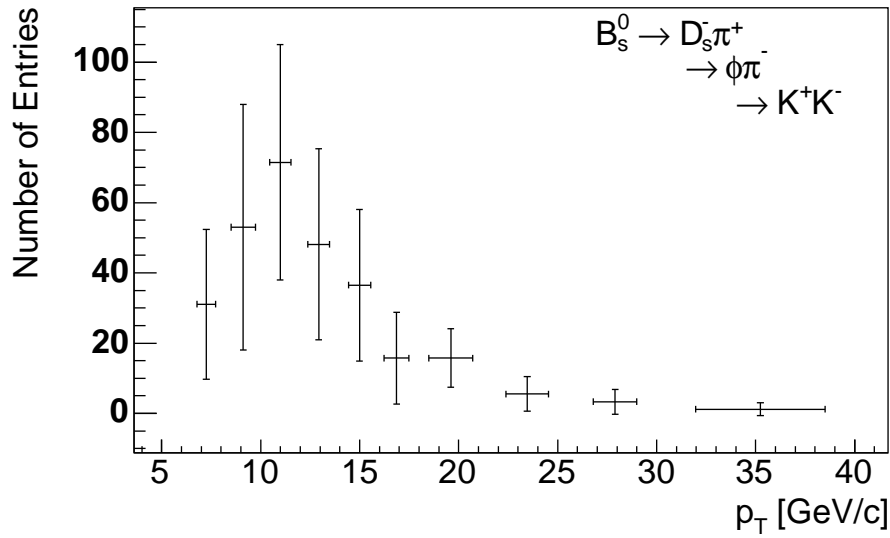


Figure 5-4: p_T spectrum for the mis-reconstructed (MR) decays in the $B_s^0 \rightarrow D_s^- \pi^+$ mode. The points are positioned horizontally using the average transverse momentum in each bin.

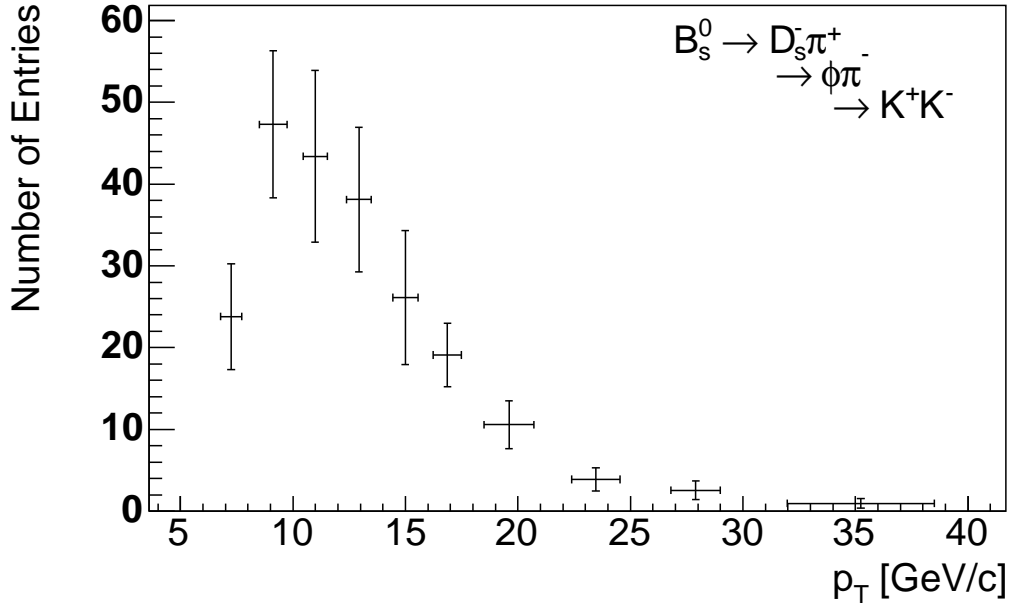


Figure 5–5: B_s hadron p_T spectrum in the signal region. The points are positioned horizontally using the average transverse momentum in each bin.

Table 5–1: $B_s \rightarrow D_s^- \pi^+$ “k” factors.

Parameter	Definition	Value
k_{41}	$\frac{N_{41}}{N_4} = \frac{\text{CB in region 1}}{\text{CB in region 4}}$	1.05 ± 0.20
k_{42}	$\frac{N_{42}}{N_4} = \frac{\text{CB in region 2}}{\text{CB in region 4}}$	1.02 ± 0.20
k_{43}	$\frac{N_{43}}{N_4} = \frac{\text{CB in region 3}}{\text{CB in region 4}}$	0.38 ± 0.10
k_{12}	$\frac{N_{12}}{N_1} = \frac{\text{PR in region 2}}{\text{PR in region 1}}$	0.39 ± 0.02
k_{13}	$\frac{N_{13}}{N_1} = \frac{\text{PR in region 3}}{\text{PR in region 1}}$	0
k_{23}	$\frac{N_{23}}{N_2} = \frac{\text{MR in region 3}}{\text{MR in region 2}}$	0.08 ± 0.01

5.1.2 $B^0 \rightarrow D^- \pi^+$ p_T spectrum

We show the different contributions to the $D\pi$ invariant mass fit in Figure 5–6. Regions 1, 2, 3 and 4 are defined from 4.5 to 4.9 GeV/c^2 , 4.9 to 5.15 GeV/c^2 , 5.2 to 5.35 GeV/c^2 and 6.0 to 7.0 GeV/c^2 , respectively. The raw p_T spectra for all regions are shown in Figure 5–7.

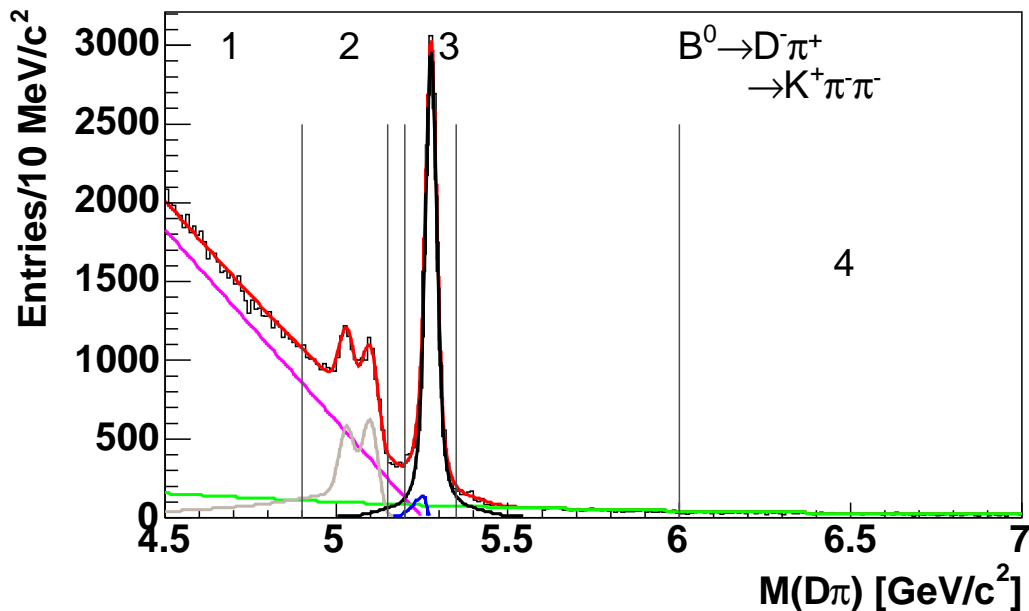


Figure 5–6: $D\pi$ invariant mass fit. The components of the fitting function, described in the previous chapter, are shown on the plot while the numbered regions used to extract the p_T spectra of the different background contributions are delimited by the vertical lines: partially reconstructed decays (1), mis-reconstructed decays (2), signal and Cabibbo suppressed decays (3) and random D -track combinations or combinatorial background (4).

For this mode, we cannot obtain the $p_T(\text{PR})$ and $p_T(\text{MR})$ using the same method as in section 5.1.1 since $p_T(\text{MR})$ contributes to $p_T(1)$ and $p_T(\text{PR})$ contributes to $p_T(2)$. We use $p_T(1)$, $p_T(2)$ and the “k” factors to obtain the spectra for the PR and MR

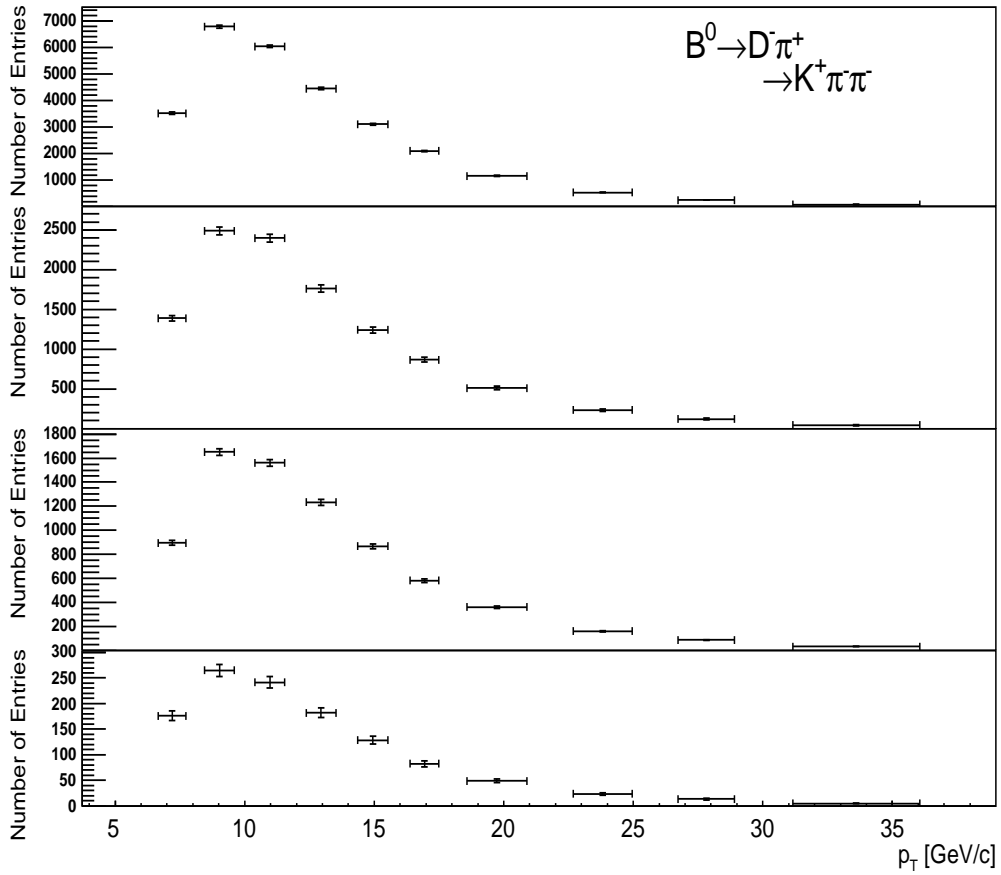


Figure 5–7: Raw p_T spectra for the invariant mass regions 1 (top) to 4 (bottom) in the $B^0 \rightarrow D^- \pi^+$ mode.

decays. This is a system of two equations with two unknowns that can easily be solved for the two p_T distributions. Moreover we use the same equation as for the B_s mode to obtain the p_T spectrum for the signal. We find

$$p_T(MR) = \frac{k_{12}}{k_{21}} \cdot \frac{p_T(2) - k_{21} \cdot p_T(1)}{1 - k_{12} \cdot k_{21}}, \quad (5.5)$$

$$p_T(PR) = p_T(1) - k_{21} \cdot p_T(MR) \quad (5.6)$$

and

$$p_T(SR) = p_T(3) - k_{43} \cdot p_T(4) - k_{13} \cdot p_T(PR) - k_{23} \cdot p_T(MR). \quad (5.7)$$

The p_T spectra for the PR and MR decays and for the B -hadron signal are shown in Figures 5–8, 5–9 and 5–10, respectively. Also, the “k” factors are compiled in Table 5–2. The contribution from the MR spectrum under the signal peak is so small that we decide to neglect it.

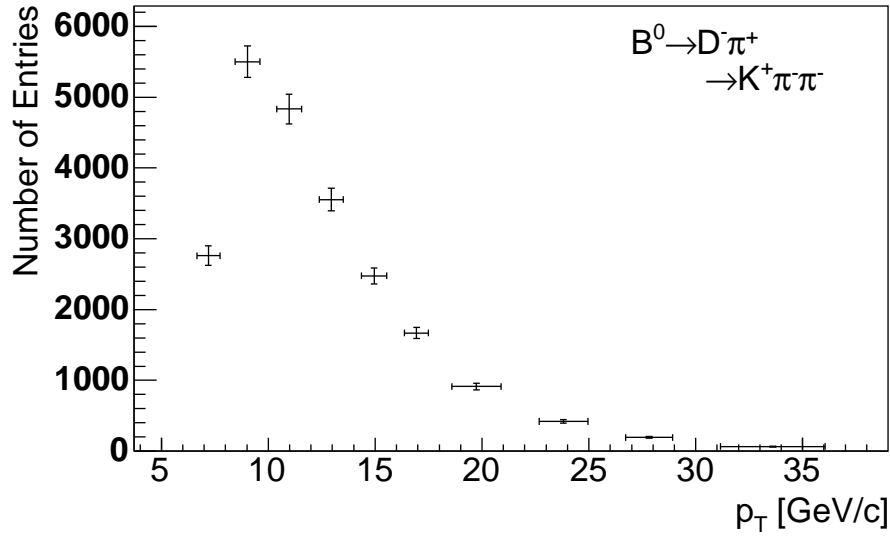


Figure 5-8: p_T spectrum for the partially reconstructed (PR) decays in the $B^0 \rightarrow D^- \pi^+$ mode. The points are positioned horizontally using the average transverse momentum in each bin.

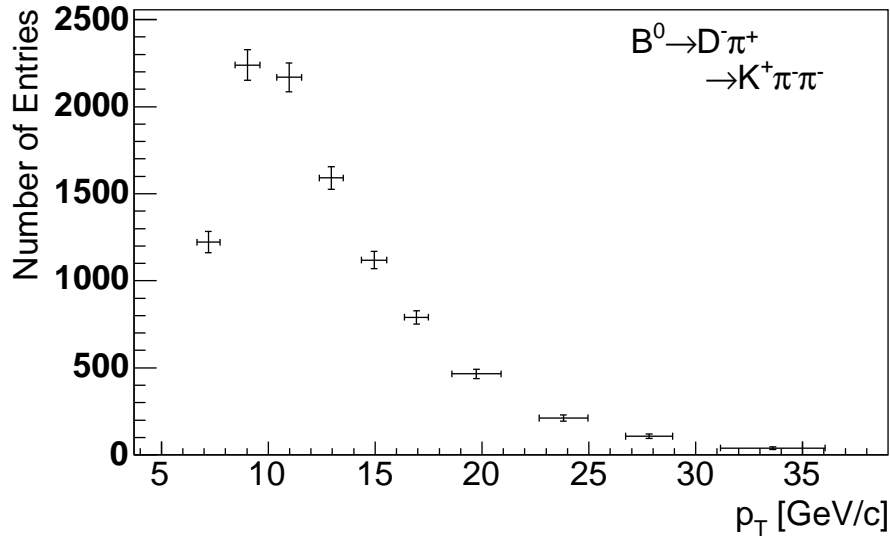


Figure 5-9: p_T spectrum for the mis-reconstructed (MR) decays in the $B^0 \rightarrow D^- \pi^+$ mode. The points are positioned horizontally using the average transverse momentum in each bin.

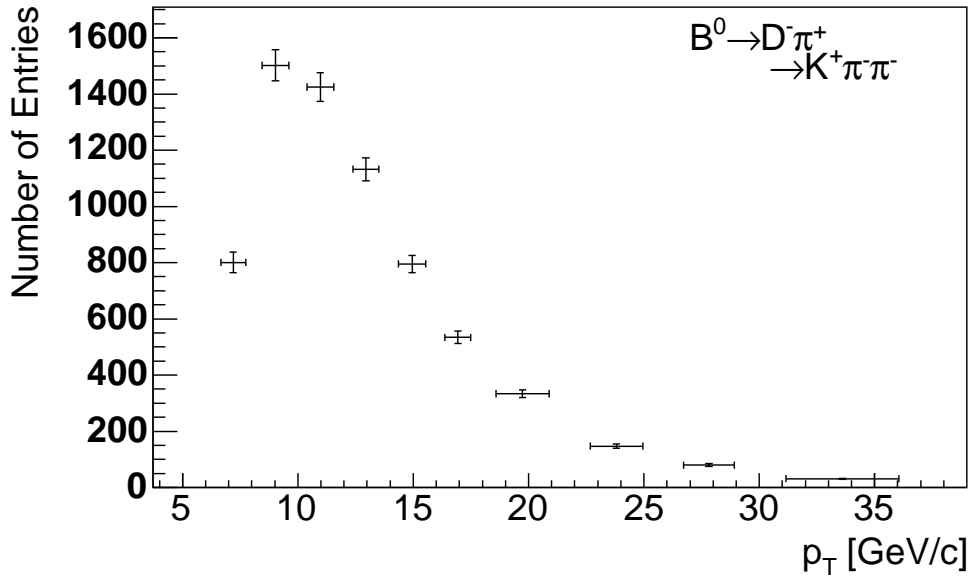


Figure 5-10: B^0 hadron p_T spectrum. The points are positioned horizontally using the average transverse momentum in each bin.

Table 5-2: $B^0 \rightarrow D^- \pi^+$ “k” factors.

Parameter	Definition	Value
k_{41}	$\frac{N_{41}}{N_4} = \frac{\text{CB in region 1}}{\text{CB in region 4}}$	2.05 ± 0.05
k_{42}	$\frac{N_{42}}{N_4} = \frac{\text{CB in region 2}}{\text{CB in region 4}}$	0.94 ± 0.03
k_{43}	$\frac{N_{43}}{N_4} = \frac{\text{CB in region 3}}{\text{CB in region 4}}$	0.45 ± 0.02
k_{12}	$\frac{N_{12}}{N_1} = \frac{\text{PR in region 2}}{\text{PR in region 1}}$	0.254 ± 0.002
k_{13}	$\frac{N_{13}}{N_1} = \frac{\text{PR in region 3}}{\text{PR in region 1}}$	0.0052 ± 0.0003
k_{21}	$\frac{N_{21}}{N_2} = \frac{\text{MR in region 1}}{\text{MR in region 2}}$	0.330 ± 0.007
k_{23}	$\frac{N_{23}}{N_2} = \frac{\text{MR in region 3}}{\text{MR in region 2}}$	$< 10^{-4}$

5.1.3 $B^0 \rightarrow D^{*-}\pi^+$ p_T spectra

We show the different contributions to the $D^*\pi$ invariant mass fit in Figure 5–11. Regions 1, 3 and 4 are defined from 4.5 to 5.1 GeV/c^2 , 5.2 to 5.35 GeV/c^2 and 6.0 to 7.0 GeV/c^2 , respectively. Note the absence of region 2, since everything below the signal region is considered as partially reconstructed background. The raw p_T spectra of regions 1, 3 and 4 are shown in Figure 5–12.

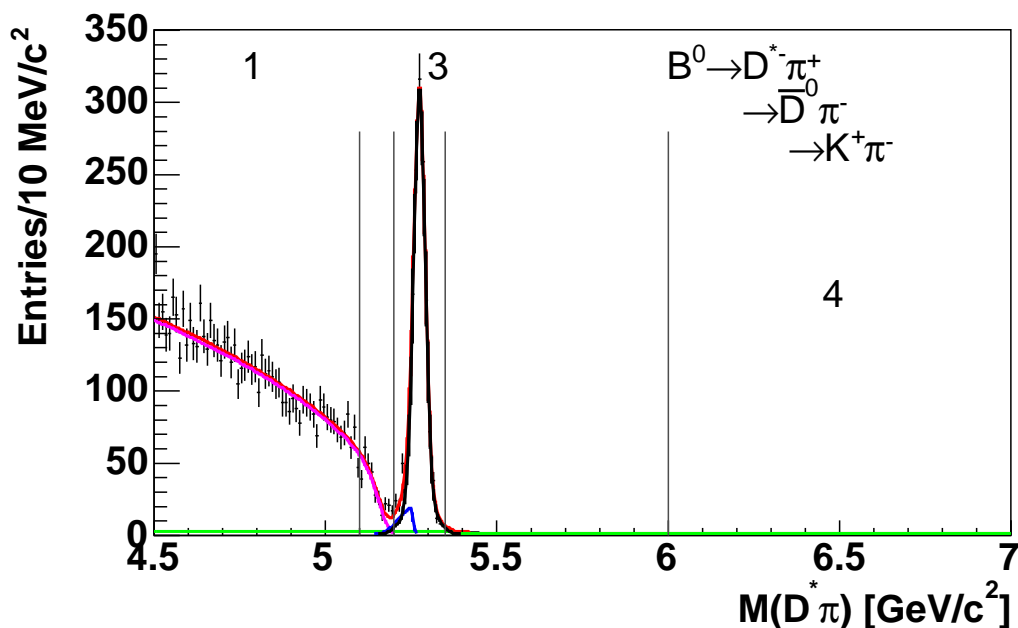


Figure 5–11: $D^*\pi$ invariant mass fit. The components of the fitting function, described in the previous chapter, are shown on the plot while the numbered regions used to extract the p_T spectra of the different background contributions are delimited by the vertical lines: partially reconstructed decays (1), signal and Cabibbo suppressed decays (3) and random D -track combinations or combinatorial background (4).

The p_T spectra for the PR decays and for the B -hadron signal are obtained using equations 5.8 and 5.9, and are shown in Figures 5–13 and 5–14 respectively. The “k”

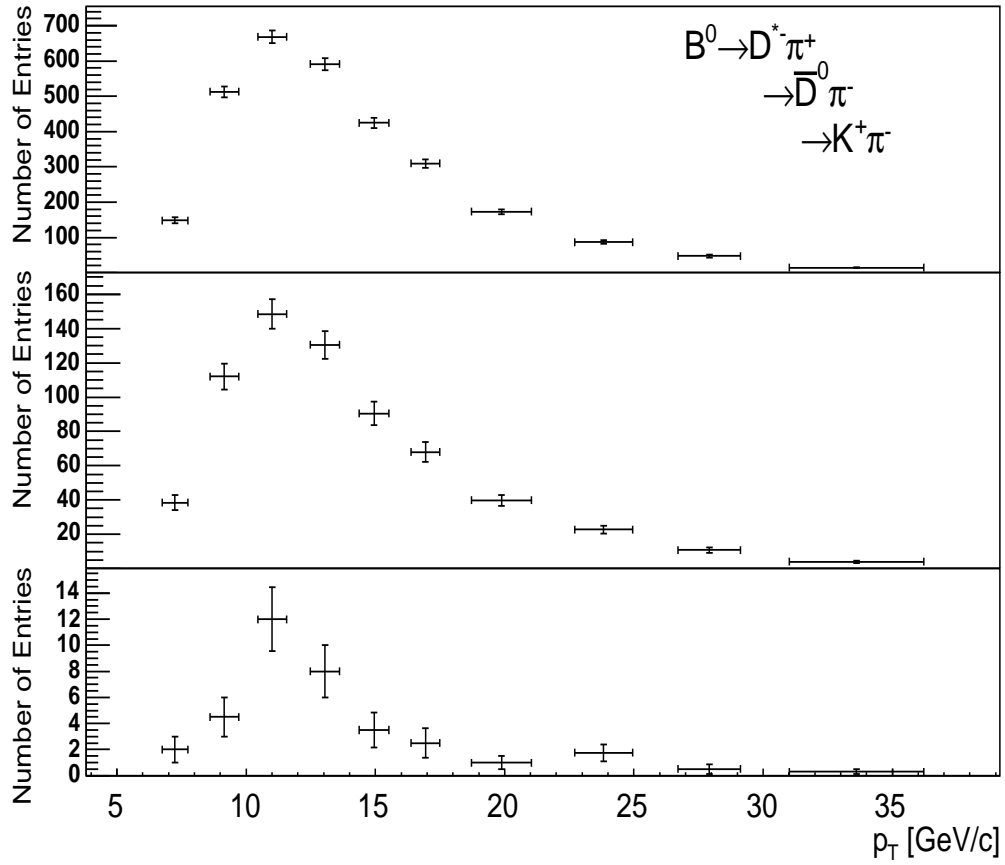


Figure 5-12: Raw p_T spectra for the invariant mass regions 1 (top), 3 (middle) and 4 (bottom) in the $B^0 \rightarrow D^{*-} \pi^+$ mode.

factors for this decay modes are displayed in Table 5-3. We can see from this table that the PR decays do not contribute to the signal region.

$$p_T(PR) = p_T(1) - k_{41} \cdot p_T(4) \quad (5.8)$$

$$p_T(SR) = p_T(3) - k_{43} \cdot p_T(4) - k_{13} \cdot p_T(PR) \quad (5.9)$$

Table 5-3: $B^0 \rightarrow D^{*-}\pi^+$ “k” factors.

Parameter	Definition	Value
k_{41}	$\frac{N_{41}}{N_4} = \frac{\text{CB in region 1}}{\text{CB in region 4}}$	1.5 ± 0.2
k_{43}	$\frac{N_{43}}{N_4} = \frac{\text{CB in region 3}}{\text{CB in region 4}}$	0.31 ± 0.07
k_{13}	$\frac{N_{13}}{N_1} = \frac{\text{PR in region 3}}{\text{PR in region 1}}$	0

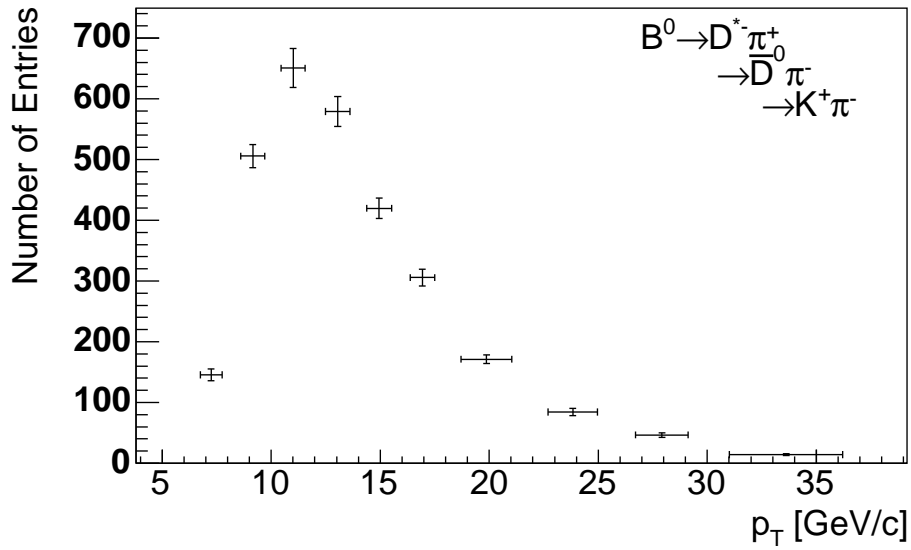


Figure 5-13: p_T spectrum for the partially reconstructed (PR) decays in the $B^0 \rightarrow D^{*-} \pi^+$ mode. The points are positioned horizontally using the average transverse momentum in each bin.

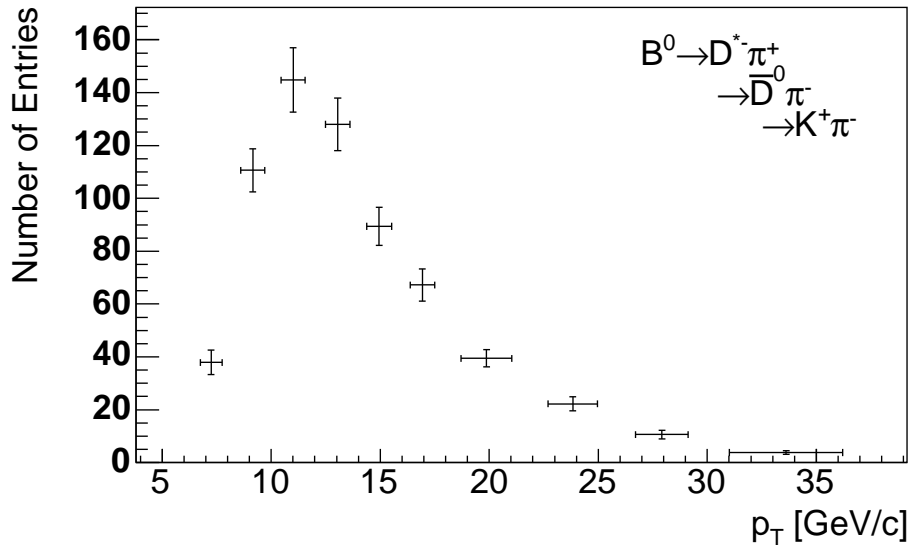


Figure 5-14: B^0 hadron p_T spectrum. The points are positioned horizontally using the average transverse momentum in each bin.

5.1.4 $\Lambda_b^0 \rightarrow \Lambda_c^+ \pi^-$ p_T spectra

We show the different contributions to the $\Lambda_c \pi$ invariant mass fit in Figure 5–15. Regions 1, 2, 3 and 4 are defined from 4.8 to 5.1 GeV/c^2 , 5.4 to 5.53 GeV/c^2 , 5.55 to 5.7 GeV/c^2 and 6.0 to 7.0 GeV/c^2 , respectively. The raw p_T spectra for all regions are shown in Figure 5–16.

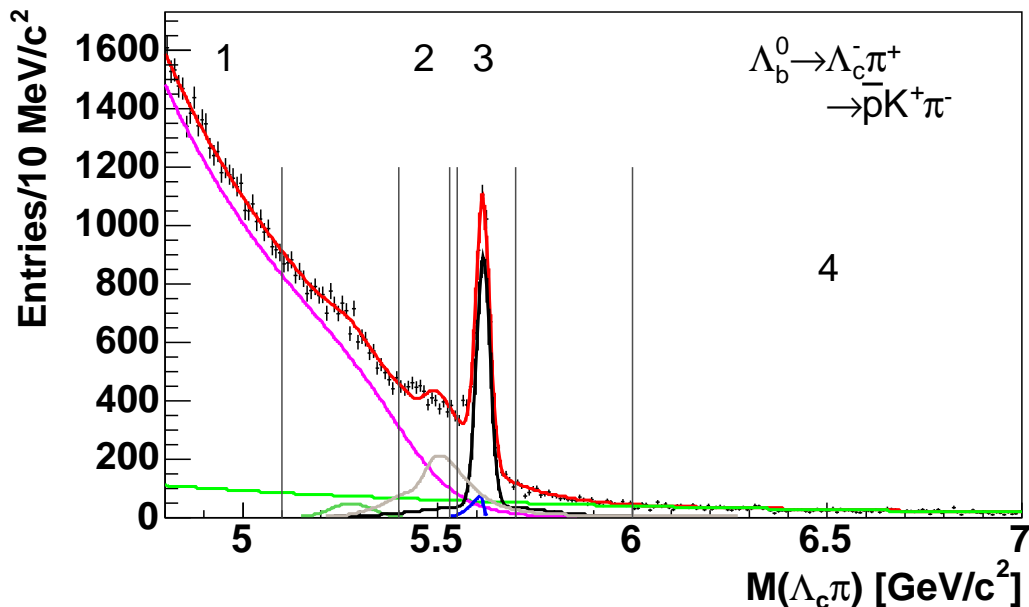


Figure 5–15: $\Lambda_c \pi$ invariant mass fit. The components of the fitting function, described in the previous chapter, are shown on the plot while the numbered regions used to extract the p_T spectra of the different background contributions are delimited by the vertical lines: partially reconstructed decays (1), mis-reconstructed decays (2), signal and Cabibbo suppressed decays (3) and random Λ_c -track combinations or combinatorial background (4).

The same method applied to obtain the p_T spectra for the $B_s^0 \rightarrow D_s^- \pi^+$ mode is used for this mode. Refer to equations 5.2, 5.3 and 5.4 to see how we obtain $p_T(\text{PR})$, $p_T(\text{MR})$ and $p_T(\text{SR})$ for this decay mode, respectively. Figures 5–17, 5–18

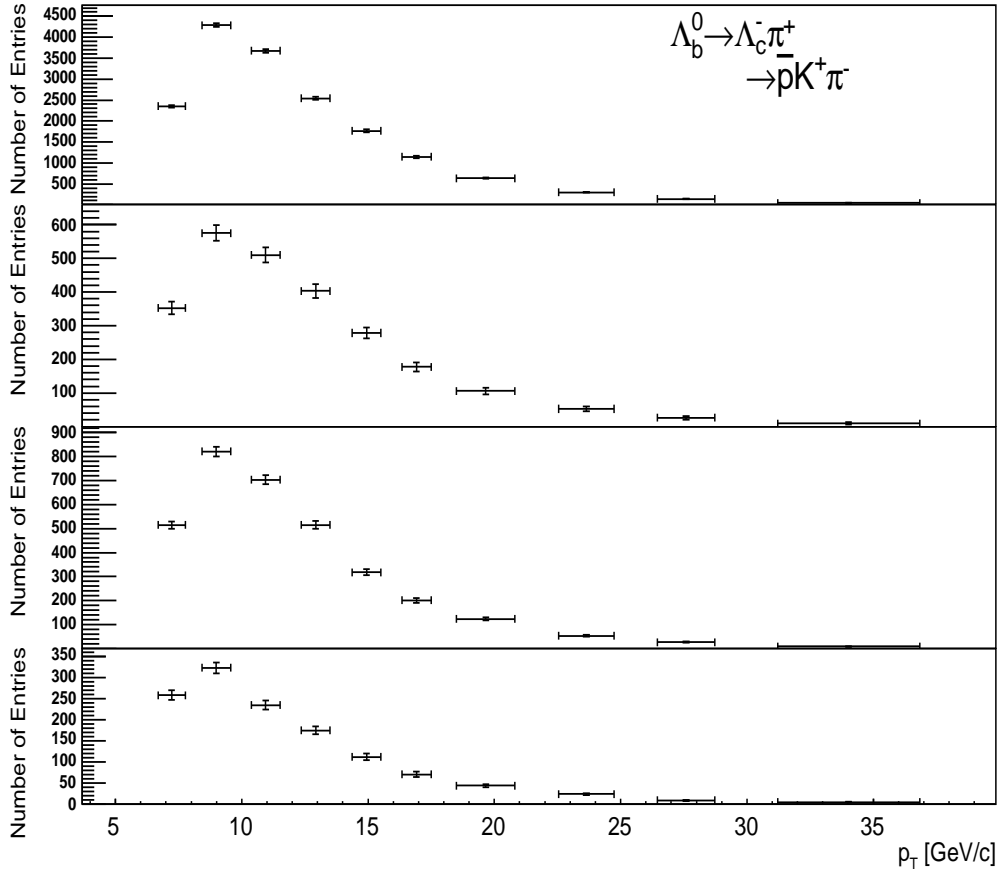


Figure 5-16: Raw p_T spectra for the invariant mass regions 1 (top) to 4 (bottom) in the $\Lambda_b^0 \rightarrow \Lambda_c^+ \pi^- \pi^-$ mode.

and 5–19 show the p_T spectrum for the PR decays, MR decays and B -hadron signal, respectively. Again, the “k” factors for this mode can be found in Table 5–4.

Table 5–4: $\Lambda_b^0 \rightarrow \Lambda_c^+ \pi^-$ “k” factors.

Parameter	Definition	Value
k_{41}	$\frac{N_{41}}{N_4} = \frac{\text{CB in region 1}}{\text{CB in region 4}}$	1.13 ± 0.03
k_{42}	$\frac{N_{42}}{N_4} = \frac{\text{CB in region 2}}{\text{CB in region 4}}$	0.31 ± 0.01
k_{43}	$\frac{N_{43}}{N_4} = \frac{\text{CB in region 3}}{\text{CB in region 4}}$	0.31 ± 0.01
k_{12}	$\frac{N_{12}}{N_1} = \frac{\text{PR in region 2}}{\text{PR in region 1}}$	0.0740 ± 0.0015
k_{13}	$\frac{N_{13}}{N_1} = \frac{\text{PR in region 3}}{\text{PR in region 1}}$	0.0155 ± 0.0007
k_{23}	$\frac{N_{23}}{N_2} = \frac{\text{MR in region 3}}{\text{MR in region 2}}$	0.58 ± 0.02

5.2 Systematics

Because of the way we have extracted the various p_T spectra for our B hadron signal and the fact that we are reporting ratios of p_T spectra, almost no sources of systematic uncertainty are present in this measurement. All the fit-parameter uncertainties were correctly propagated when subtracting different contributions from our p_T spectra. In doing so, the statistical uncertainties in the final p_T spectra embody the systematic effects due to fits of the invariant mass distributions. A more detailed analysis of the systematic uncertainties is under way.

5.3 Monte Carlo

We use **Bgenerator** [41] to generate MC events for this analysis. Bgenerator generates a single b quark following the theory from Nason, Dawson and Ellis

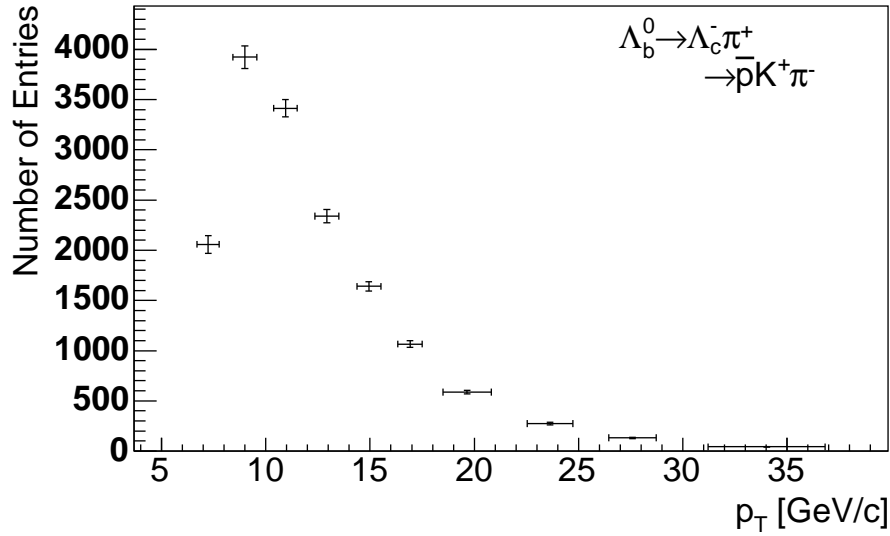


Figure 5-17: p_T spectrum for the partially reconstructed (PR) decays in the $\Lambda_b^0 \rightarrow \Lambda_c^+ \pi^-$ mode. The points are positioned horizontally using the average transverse momentum in each bin.

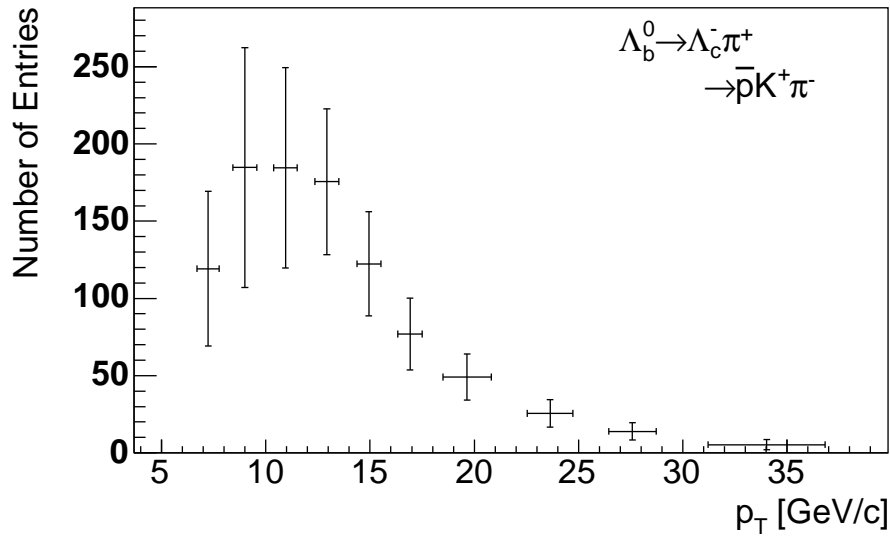


Figure 5-18: p_T spectrum for the mis-reconstructed (MR) decays in the $\Lambda_b^0 \rightarrow \Lambda_c^+ \pi^-$ mode. The points are positioned horizontally using the average transverse momentum in each bin.

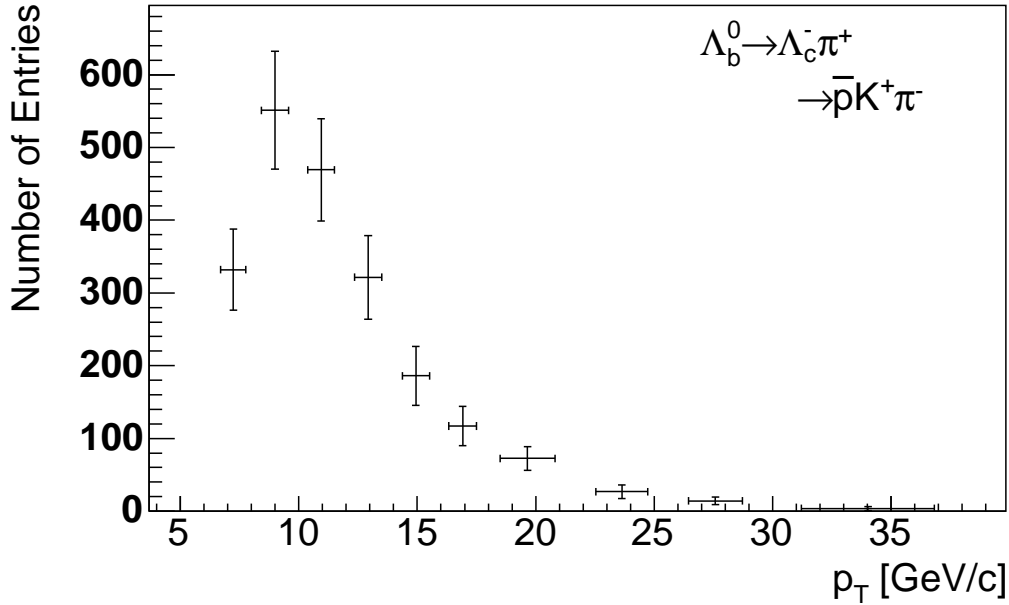


Figure 5–19: Λ_b hadron p_T spectrum. The points are positioned horizontally using the average transverse momentum in each bin.

(NDE) [42]. The mass of the b quark is set to $4.75 \text{ GeV}/c^2$. The b quarks are generated with a p_T threshold of $4.0 \text{ GeV}/c$ over the rapidity range of $|y| < 2.0$. For the B meson MC samples, the b quarks are fragmented into B mesons using the CDF default Peterson fragmentation parameter [9], ϵ_B , set to 0.006. The B hadrons are then decayed using the best available descriptions of the decay dynamics using the EvtGen program [43]. We apply the same geometric and kinematic selection to the simulated events as we apply to reconstruct our signal in data. Since there is a 4σ discrepancy between the Λ_b baryon p_T spectrum obtained from MC and data [19], the b quarks need to be generated using a re-weighted p_T spectrum that reproduces the data for this particular channel.

5.4 Results

The background subtracted ratios of p_T spectra $N(B_s \rightarrow D_s\pi)/N(B^0 \rightarrow D\pi)$, $N(B^0 \rightarrow D^*\pi)/N(B^0 \rightarrow D\pi)$ and $N(\Lambda_b \rightarrow \Lambda_c\pi)/N(B^0 \rightarrow D\pi)$ for MC (black circle) and data are shown in Figures 5–20, 5–21 and 5–22, respectively.

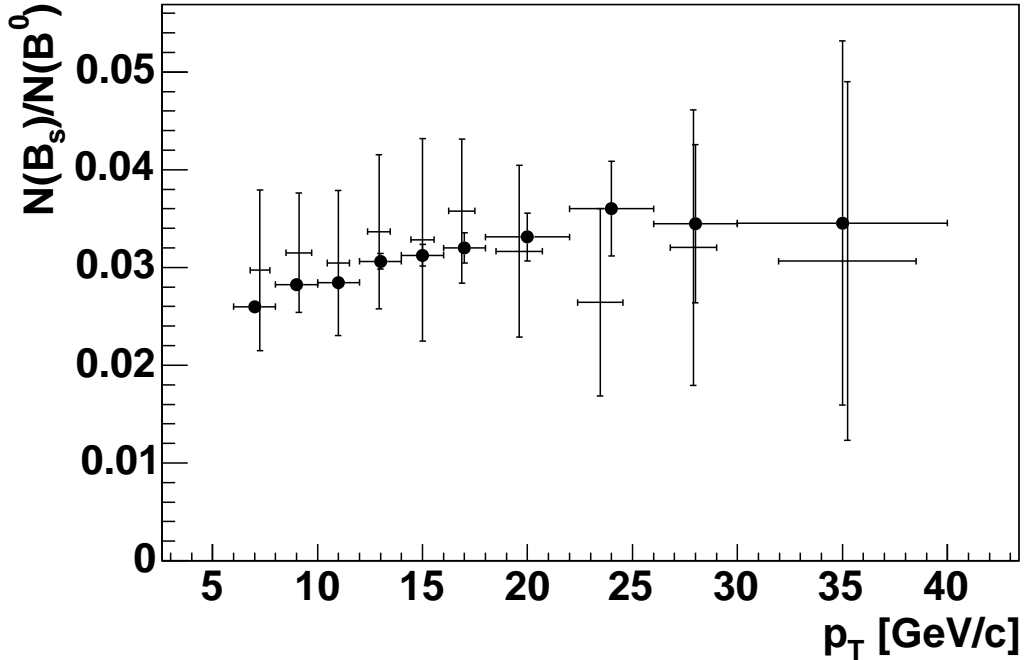


Figure 5–20: Ratios of B_s and B^0 p_T spectra for both MC (black circle) and data.

The ratio plots for both data and MC are not corrected for acceptance and reconstruction efficiency. We expect Figure 5–21 to give a flat ratio after these corrections as the parent particle for the two decays is the same. We can see that we are on the right track as the MC generated for the corresponding decay modes from data gives us a similar ratio of p_T spectra. The uncertainties on the MC are not realistic as the track combinations for the MC samples are not selected the same way as in data.

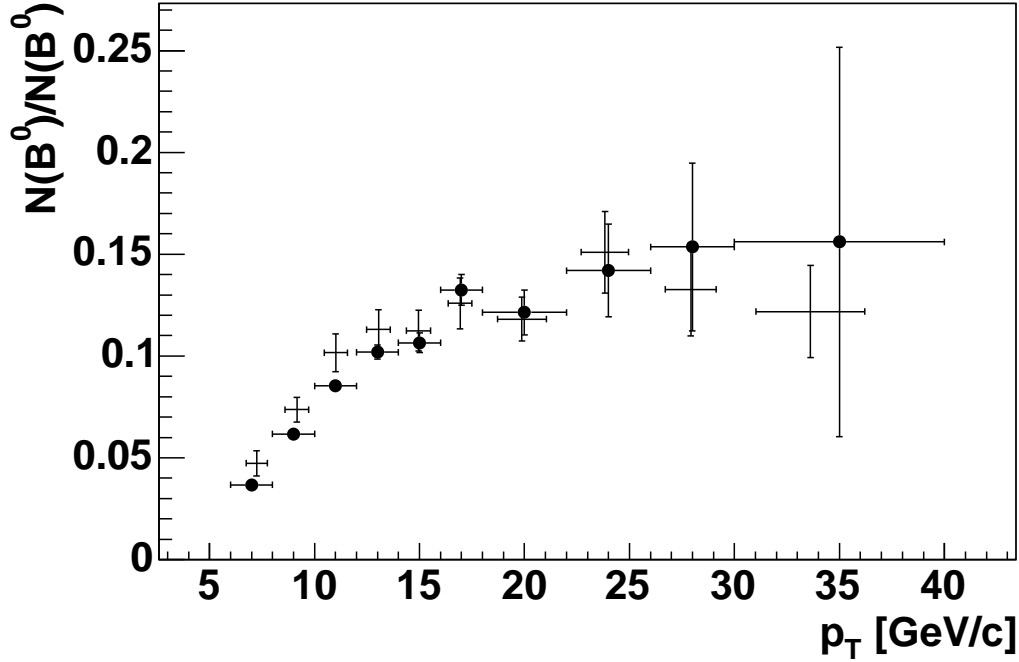


Figure 5-21: Ratios of $B^0 \rightarrow D^*\pi$ and $B^0 \rightarrow D\pi$ p_T spectra for both MC (black circle) and data.

Nevertheless, the shapes obtained for the MC ratios do make a good comparison with our data as this selection is done consistently across all decay modes and the same analysis cuts applied on data are used. It is also worth noting that the ratios obtained using the MC are scaled down to the data to fit on the same plot. This difference between data and MC is expected as we did not generate the same number of events across all the decay modes. Because of the nature of our measurement, most of the detector effects cancel out. It has been shown that the difference between generator level MC and full MC simulation is of the order of about 5% [19]. A full

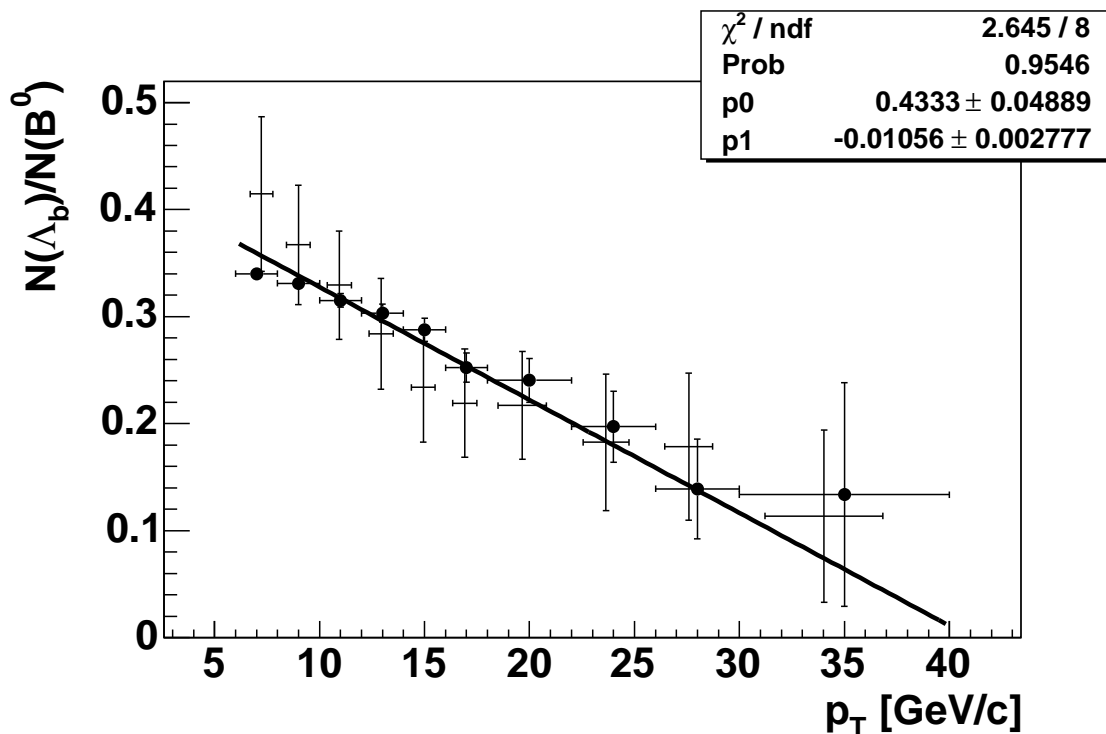


Figure 5–22: Ratios of Λ_b and B^0 p_T spectra for both MC (black circle) and data. We fit the data points to a straight line and obtain a slope approximately 3.8σ away from zero.

simulation MC study will be done for this analysis later and is not discussed in this thesis.

Based on our studies, the comparison of data to MC tells us that the MC qualitatively reproduces the ratio of p_T distributions. Because of this agreement, the effects due to acceptance and resolutions largely cancel in the ratio. Therefore, we can interpret the raw ratios of p_T distributions and come to some conclusions:

- B_s and B^0 are produced with similar p_T distributions.

- Λ_b are produced “softer” (at lower p_T) than the B^0 , as suggested by the statistically significant negative slope in Figure 5–22.

If we follow equation 1.5, we note that $\sigma(p\bar{p} \rightarrow b\bar{b})$ is common to the production of all B hadrons. We can then infer that the observed p_T dependence occurs in the fragmentation process. This represents a departure from the assumptions applied in the previous measurements at the Tevatron [15] and LEP [16] [17] for the fragmentation to the Λ_b baryon.

CHAPTER 6

Conclusion

In the course of this analysis we reduced 1.9 fb^{-1} of data, obtained with the CDF-II detector, by a factor of 1000 and reconstructed the fully hadronic exclusive decay modes

- $B_s^0 \rightarrow D_s^- \pi^+$, where $D_s^- \rightarrow \phi \pi^-$, $\phi \rightarrow K^+ K^-$;
- $B^0 \rightarrow D^- \pi^+$, where $D^- \rightarrow K^+ \pi^- \pi^-$;
- $B^0 \rightarrow D^{*-} \pi^+$, where $D^{*-} \rightarrow \bar{D}^0 \pi^-$, $\bar{D}^0 \rightarrow K^+ \pi^-$;
- $\Lambda_b^0 \rightarrow \Lambda_c^+ \pi^-$, where $\Lambda_c^- \rightarrow \bar{p} K^+ \pi^-$.

We reconstructed 473 ± 42 $B_s^0 \rightarrow D_s^- \pi^+$, 15206 ± 203 $B^0 \rightarrow D^- \pi^+$, 1483 ± 45 $B^0 \rightarrow D^{*-} \pi^+$ and 4444 ± 297 $\Lambda_b^0 \rightarrow \Lambda_c^+ \pi^-$ candidates for this analysis. The Λ_b and B_s candidates in this study represent the world's largest fully reconstructed sample of these hadrons.

We then extracted the p_T spectrum for each B hadron using a sideband subtraction method. We fitted each charm+ π invariant mass spectrum using a composite function that described the overall shape of the spectrum. Each global function was composed of many functional forms, each of which described a component of the background, and the signal. We obtained a purified p_T spectrum for each B hadron and evaluated the uncertainties associated with each spectrum. We then compared the p_T distributions of the B_s and Λ_b hadrons to the spectrum of the B^0 meson. We can draw two conclusions from these measurements:

1. The B_s p_T distribution is similar to that of the B^0 .
2. The Λ_b p_T distribution is softer than that of the B^0 .

The technique used to extract the B -hadron p_T spectra measures background shapes from data rather than predicting background shapes from simulation. As a result, our uncertainties are dominantly “statistical” in nature and may be reduced with more data. The results obtained can only improve as the size of the data sample increases; the present data sample is already more than ten times bigger than that used in [19]. Propagation of uncertainties is a key factor for this analysis as it allows us to describe most of our uncertainties as statistical. Because of this, all our results are expected to have small systematic uncertainties.

6.1 Future Work

Several things remain to be done as we have yet to extract a quantitative measurement of the p_T dependence of the production cross sections:

$$\frac{\frac{d\sigma}{dp_T}(p\bar{p} \rightarrow \Lambda_b^0 X)}{\frac{d\sigma}{dp_T}(p\bar{p} \rightarrow B^0 X)} \quad \text{and} \quad \frac{\frac{d\sigma}{dp_T}(p\bar{p} \rightarrow B_s^0 X)}{\frac{d\sigma}{dp_T}(p\bar{p} \rightarrow B^0 X)}. \quad (6.1)$$

We need a good simulation of data to correct for acceptance and efficiencies using full detector simulation. Systematic uncertainties will arise from this correction and we will need to take them into account properly. An optimization of the B -hadron kinematic fit probability and impact parameter ($d_0(B\text{hadron})$) cuts will also be done.

This measurement has relevance to many aspects of the larger field. Indeed, most analyses in B physics require fragmentation knowledge in their simulations. This measurement is an important empirical probe of non-perturbative QCD and

addresses a possible fundamental difference in particle production between lepton and hadron colliders. This work will also lead to improved measurements of B_s branching ratios such as $B_s \rightarrow \mu\mu$ [44] and $B_s \rightarrow \mu\mu\phi$ [45] [46], which are of interest in searches for physics not described by the Standard Model.

REFERENCES

- [1] J. Schwinger, “Quantum Mechanics,” Dover Publications Inc., New York (1958).
- [2] S. Weinberg, Phys. Rev. Lett. **19**, 1264 (1967);
A. Salam, “Elementary Particle Theory,” ed. N. Svartholm, Almquist and Wilsells, Stockholm, p. 367 (1969);
S. L. Glashow, J. Iliopoulos, and L. Maiani, Phys. Rev. D **2**, 1285 (1970).
- [3] G. L. Kane, “Modern Elementary Particle Physics,” (Reading, USA: Addison-Wesley, 1987).
- [4] J. M. Pursley, “Discovery and measurement of excited b hadrons at the Collider Detector at Fermilab,” Ph. D. Thesis, (2007).
- [5] A. F. Falk, “The heavy quark expansion of QCD,” arXiv:hep-ph/9610363, (1996).
- [6] A. V. Manohar and M. B. Wise, “Heavy quark physics,” Camb. Monogr. Part. Phys. Nucl. Phys. Cosmol. **10**, 1 (2000).
- [7] V. G. Kartvelishvili, A. K. Likhoded and V. A. Petrov, Phys. Lett. **78B**, 615 (1978).
- [8] M. G. Bowler, Z. Phys. C **11**, 169 (1981).
- [9] C. Peterson, D. Schlatter, I. Schmitt and P.M. Zerwas, Phys. Rev D **27**, 105 (1983).
- [10] B. Andersson, G. Gustafson, G. Ingelman and T. Sjöstrand, Phys. Rep. **97**, 32 (1983).
- [11] P.D.B. Collins and T.P. Spiller, J. Phys. G **11**, 1289 (1985).
- [12] A. T. Warburton, “A Study of exclusive nonleptonic decays of B mesons into final states of strange mesons and 1S or 2S charmonia,” Ph.D. Thesis, University of Toronto, (1998).

- [13] J. Chrin, “Upon the Determination of Heavy Quark Fragmentation Functions in e^+e^- annihilations,” *Z. Phys. C* **36**, (1987).
- [14] K. Abe *et al.*, “Measurement of the b -Quark Fragmentation Function in Z^0 Decays,” *Phys. Rev. D* **65**, 092006 (2002).
- [15] K. Gibson, “Measurement of the Relative Fragmentation Fractions of \bar{B} Hadrons,” PhD Thesis, Carnegie Mellon University, (2005).
- [16] P. Abreu *et al.*, DELPHI Collaboration, “Lifetime and production rate of beauty baryons from Z decays,” *Z. Phys. C* **68**, 375 (1995).
- [17] R. Barate *et al.*, ALEPH Collaboration, “Measurement of the b baryon lifetime and branching fractions in Z decays,” *Eur. Phys. J.* **C2**, 197 (1998).
- [18] Heavy Flavor Averaging Group, E. Barberio *et al.*, “Averages of b -hadron properties at the end of 2006,” arXiv:0704.3575v1 [hep-ex] (2007).
- [19] S-S Yu, “First Measurement of the Ratio of Branching Fractions $BR(\Lambda_b \rightarrow \Lambda_c \mu \nu)/BR(\Lambda_b \rightarrow \Lambda_c \pi)$ at CDF II,” Ph.D. Thesis, University of Pennsylvania, (2005).
- [20] S.-S. Yu, Private Communication.
- [21] G. Buchalla and A. J. Buras, *Nucl. Phys.* **B400**, 225 (1993).
- [22] A. J. Buras, *Phys. Lett.* **B566**, 115 (2003).
- [23] P. Colangelo, F. De Fazio, R. Ferrandes and T. N. Pham, *Phys. Rev. D* **73**, 115006 (2006).
- [24] F. Kruger, J. Matias, *Phys. Rev. D* **71**, 094009 (2005).
- [25] T. M. Aliev, A. Ozpineci and M. Savci, *Eur. Phys. J.* **C29**, 265 (2003).
- [26] D. A. Demir, K. A. Oliv and M. B. Voloshin, *Phys. Rev. D* **66**, 034015 (2002).
- [27] D. Acosta *et al.*, “Measurement of the J/ψ meson and b -hadron production cross sections” *Phys. Rev. D* **71**, 032001 (2005).
- [28] C. S. Hill *et al.* [CDF Collaboration], “Operational experience and performance of the CDF II silicon detector,” *Nucl. Instrum. Meth. A* **530**, 1 (2004).

- [29] A. Sill *et al.* [CDF Collaboration], “CDF Run II silicon tracking projects,” Nucl. Instrum. Meth. A **447**, 1 (2000).
- [30] A. A. Affolder *et al.* [CDF Collaboration], “Intermediate silicon layers detector for the CDF experiment,” Nucl. Instrum. Meth. A **453**, 84 (2000).
- [31] W. Bokhari *et al.*, “The ASDQ ASIC,” CDF internal note, **CDF 4515** (1998).
- [32] S. Donati and G. Punzi, “Two Track trigger with full SVT simulation,” CDF internal note, **CDF 3780** (1996).
- [33] S. Donati, “CDF II Detector and Trigger for B Physics,” CDF internal note, **CDF 8391** (2006).
- [34] P. Roy, R. Snihur, R. J. Tesarek, E. Vataga and A. Warburton, “Datasets for Fully Reconstructed Decays of B^0 , B_s and Λ_b Hadrons Using the TTT,” CDF internal note, **CDF 8805** (2007).
- [35] J. Marriner, “Secondary Vertex Fit with Mass and Pointing Constraints (CTVMFT),” CDF internal note, **CDF 1996** (1993).
- [36] W.-M. Yao *et al.* (Particle Data Group), J. Phys. G **33**, 1 (2006).
- [37] I. Gorelov *et al.*, “ Λ_b Data Sample and Mass Fit with Two Displaced Track Trigger Using 1 fb^{-1} ,” CDF internal note, **CDF 8395**, (2006).
- [38] I.K. Furic, “Measurement of the Ratio of Branching Fractions $\text{BR}(B_s \rightarrow D_s^- \pi^+)/\text{BR}(B^0 \rightarrow D^- \pi^+)$ at CDF-II,” PhD Thesis, Massachusetts Institute of Technology, (2004).
- [39] S.-S. Yu, R.J. Tesarek, D. Litvinsev, J. Heinrich and N. Lockyer, “Ratio of Λ_b Semileptonic to Hadronic Branching Fractions in the Two Track Trigger,” CDF internal note, **CDF 7559**, (2005).
- [40] G. Cowan, “Statistical Data Analysis,” Oxford University Press, p. 37-39 (1998).
- [41] K. Anikeev, P. Murat and C. Paus, “Description of Bgenerator II,” CDF internal note, **CDF 5092** (1999).
- [42] P. Nason, S. Dawson and R.K. Ellis, Nucl. Phys. **B303** (1988); Nucl. Phys. **B327**, 49 (1989).

- [43] W. Bell, J. P. Fernandez, L. Flores, F. Wuerthwein and R. J. Tesarek, “User Guide for EvtGen @ CDF,” CDF internal note, **CDF 5618**, (2001); J. Beringer *et al.*, “User Guide for the New EvtGen @ CDF,” CDF internal note, **CDF 7917**, (2005).
- [44] T. Aaltonen *et al.*, ”Search for $B_s \rightarrow \mu^+ \mu^-$ and $B_d \rightarrow \mu^+ \mu^-$ Decays with 2 fb^{-1} of $p\bar{p}$ Collisions,” Phys. Rev. L **100**, 101802 (2008).
- [45] S. Farrington and R. Oldeman, “Search for the Rare Decays $B^+ \rightarrow \mu^+ \mu^- K^+$, $B^0 \rightarrow \mu^+ \mu^- K^{*0}$ and $B_s \rightarrow \mu^+ \mu^- \phi$,” CDF internal note, **CDF 8543** (2006).
- [46] W. M. Abazov *et al.*, “Search for the rare decay $B_s^0 \rightarrow \phi \mu^+ \mu^-$ with the D0 detector,” Phys. Rev. D **74**, 031107(R) (2006).